MORPHOLOGY AND OPTICAL PROPERTY CONTROL OF ELECTRODEPOSITED ZINC OXIDE

TINGTING REN

Morphology and Optical Property Control of Electrodeposited Zinc Oxide

by

Tingting Ren

A Thesis Submitted in Partial Fulfilment of
the Requirements for the Degree of

Master of Science

Department of Physics and Physical Oceanography
Memorial University of Newfoundland

September, 2006

St. John's Newfoundland

Abstract

Active-matrix liquid crystal displays (LCDs) can be made brighter and more efficient by using optically transparent thin film transistors (TFTs). Economical production, small size, and control of defects are all essential factors in introducing transparent semiconductors into TFT device applications. As potential candidates for TFT applications, semiconducting ZnO thin films (300 nm to 2 μm thickness) were economically synthesized on stainless steel substrates using electrodeposition in this thesis work. Scanning Electron Microscopy images show that applied deposition voltage affects ZnO crystallite morphologies and deposition time influences crystallite sizes. Ultraviolet-Visible reflectance measurements show that the ZnO bandgap energy increases with more negative deposition potentials, and varies inversely with film thickness and aging time, ranging from 3.1 eV to 3.4 eV. One of the likely reasons for the bandgap energy dependence with film thickness, applied potential, and aging time is a hydrogen-induced Moss-Burstein effect. Hydrogen is evolved from the aqueous solution during electrodeposition, and it can be incorporated as an electron donor and increase the bandgap energy. Defects also appear to play a role in restricting hydrogen diffusion.

Acknowledgements

This thesis would not have been possible without help and support from many people. I would like to express my gratitude here.

First of all, I would like to sincerely thank my advisor Dr. Poduska who has been so supportive, helpful, and patient during these two years. Without her guidance and inspiration, this thesis would have never been written.

I would like to thank Shawn Chatman in my group who helped me during this two years with my experiments and research. I would also like to thank Holly Baker and Bryan Jerrett for their contribution, as they synthesized some of the samples and analyzed them. I would like to thank the following people for letting me use their instruments: Dr. K. Nag of the Department of Biochemistry (Raman spectroscopy), Dr. R. Mason and Mrs. H. Gillespie of the Department of Earth Sciences (X-Ray Diffractometry), Mrs. L. Lee of the Department of Biology (Scanning Electron Microscopy), and L.G.B. Thompson of the Department of Chemistry (Diffuse reflectance Ultraviolet-Visible spectroscopy).

Finally, I want to thank my parents who gave me birth and strength. Thank you for your unconditional love and support, without which I would have never made it this far in my work. I would also like to thank all my friends inside and outside the Department for their help.

Contents

List of Tables

List of Figures

Chapter 1

Introduction

According to Moore's law, the size of a transistor decreases by half every eighteen months [1]. Moore's law has traditionally functioned quite well. However, in the last five years, the rate of decrease has slowed down because some transistor layers have already come to thicknesses of several atoms [2]. It is difficult to go beyond this natural size barrier and decrease transistor dimensions further. In addition, one also gets new (quantum) effects at these length scales. While transistor speed had always been improved by reducing the transistor size for smaller electrical resistance, a better way of keeping up the "faster, cheaper, smaller" trend is to use different transistor materials or preparation methods to increase transistor speeds, increase effective density of integrated circuits, and decrease production costs.

One type of transistor which shows potential to benefit from different materials and preparation methods is the thin film transistor (TFT). Thin film transistors

belong to the field effect transistor category and only have one channel layer (n-type or p-type semiconductor) responsible for the transistor current flow. Figure 1.1 is a schematic illustration of a typical TFT structure [3] which has four layers of thin films. A potential is applied between the conductive gate layer and conductive source layer to induce an electric field in the channel layer. The gate insulator layer blocks the current leakage between the channel layer and the conductive gate layer. When applying a potential between the source and drain layers (V_{SD}), the drain current can be controlled by the electric field in the channel layer or the gate-source voltage (V_{GS}). Therefore, the thin film layers can function as a transistor.

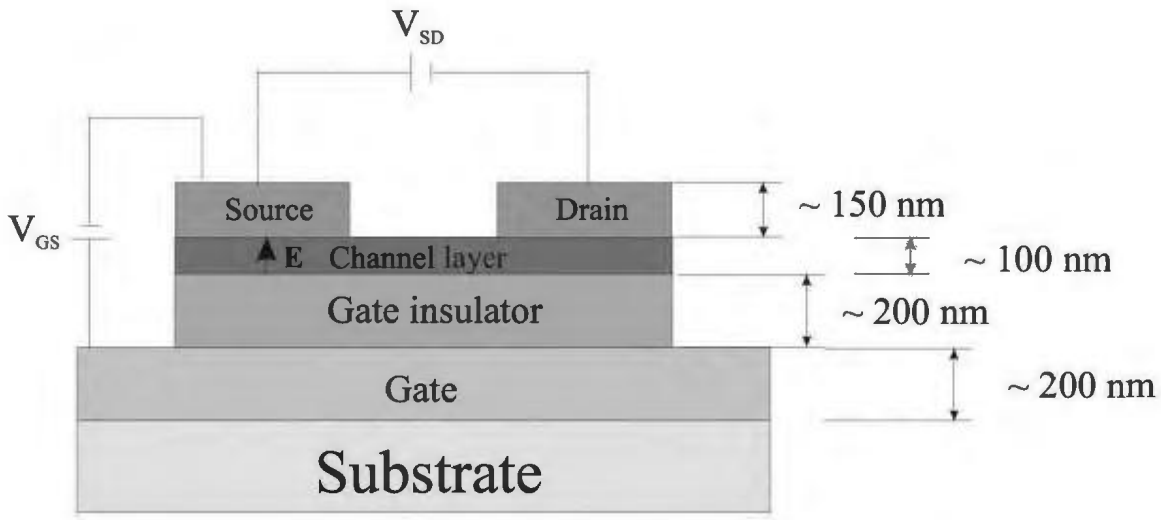

Figure 1.1: Schematic illustration of a thin film transistor.

Channel layers in most TFTs are amorphous Si, but ZnO is a promising candidate to replace it [4, 5]. ZnO can make active-matrix liquid crystal displays (LCD) more

efficient and brighter than the traditional amorphous Si [6]. The ZnO channel layer has high channel mobility, up to 7 $cm^2 \cdot s/V$ [7], compared with amorphous Si channel mobilities, which are normally 0.5 – 1 $cm^2 \cdot s/V$ [8]. In addition, ZnO based TFTs have high optical transparency (above 80% in the visible part of the light spectrum [3]), but amorphous Si TFTs are relatively opaque.

ZnO also shows potential for a large variety of other opto-electronic applications such as light emitting diodes (LED) [9], laser diodes [9], ceramic varistors [10], piezo-electric transducers [10], and photovoltaics [11]. In thin film solar cells [12], zinc oxide is widely used as a transparent thin film window material because of its large optical bandgap energy (3.3 eV) at room temperature [13]. Moreover, in light emitting devices, different doping levels in ZnO can make the emitted light intensity tunable [14]. Therefore, ZnO is a useful material to study, especially in thin film form.

ZnO, also called zincite, has a wurtzite crystal structure as shown in Figure 1.2. Every Zn atom has four O nearest-neighbours and every O atom has four Zn nearest neighbours. The Zn and O sublattices are hexagonal Bravais lattices. The two sublattices penetrate each other along the c-axis to form a wurtzite-type structure with space group $P6_3mc$ and two formula units per cell (a=b=3.25 Å, c=5.21 Å, α=β=90°, γ=120°). Because the wurtzite structure is not centrosymmetric, ZnO is also a piezo-electric material.

ZnO thin films have been traditionally prepared with high vacuum based techiques such as magnetron sputtering [11], pulsed laser deposition [15], and molecular beam

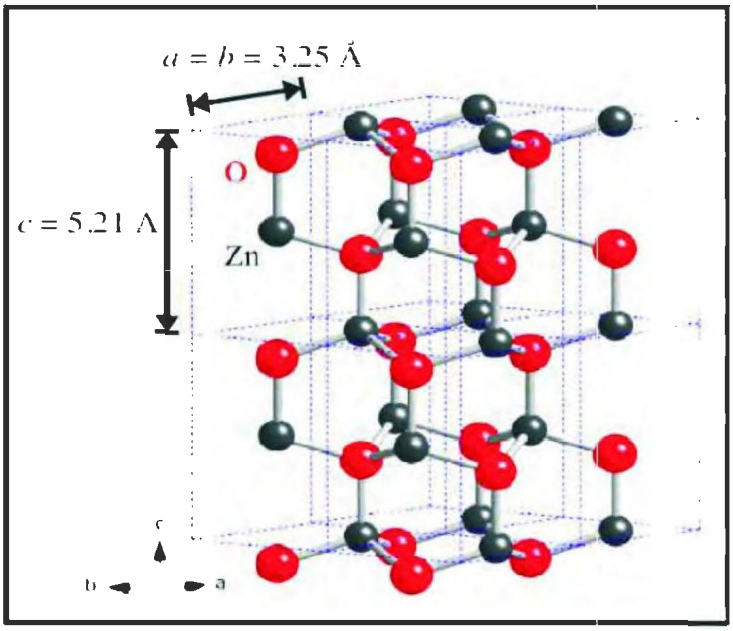

Figure 1.2: Zinc oxide wurtzite crystal structure.

epitaxy (MBE) [16]. Drastic temperature change is required for thermal bath deposition to precipitate ZnO out of supersaturated solutions [17], and high temperature is required for thermal oxidation of Zn metallic films [18]. In comparison, electrodeposition can occur at lower temperatures (25 – 90 °C) and ambient pressure [19]. Preparation without high temperature and high vacuum is more convenient and economical. Furthermore, electrodeposition is suitable for large area coating [20], which is especially useful for solar cell applications.

In reports of ZnO electrodeposition, the parameters influencing ZnO crystal morphology and opto-electronic properties include substrate [21], deposition time [12], applied potential [19], temperature [22], concentration of electrolyte [23], and addi-

tives to the electrolyte [17]. Some literature reports very similar electrodeposition parameters, but with rather different ZnO crystal morphology or optical properties. For example, Mahalingam *et al.* [24] reported that large ($\sim$ 10 μm) and edge-oriented (c-axis parallel to substrate) ZnO platelet crystals were electrodeposited on doped tin oxide/glass at –1.10 V *vs.* a Saturated Calomel reference Electrode (SCE) from 0.10 M $Zn(NO_3)_2$. In contrast, Xu *et al.* [25] reported that smaller ($\sim$ 0.5 μm diameter) and well-aligned hexagonal particles with c-axis perpendicular to doped tin oxide/glass can be electrodeposited with the same applied potential from a less concentrated (0.05 M $Zn(NO_3)_2$) electrolyte. Beyond adjusting electrolyte composition, Aghamalyan *et al.* [26] found that both bandgap energy and XRD (002) Bragg peak width were decreased using thermal annealing after preparing ZnO thin films by MBE. Therefore, small changes in certain preparation parameters can play a large role in influencing both morphologies and optical properties of electrodeposited ZnO thin films.

One of the fundamental optical properties of ZnO is the optical bandgap energy (E_g). Zinc oxide bandgap energies have been reported to range from 2.8 eV to 4.0 eV [27]. Typical ways of tuning the zinc oxide bandgap energy are doping with transition metals such as Cd and Mg [27, 28], varying film thickness [12], tuning the deposition potential [12, 29], changing the substrate [30], and modifying the crystal size [31]. The dependence of bandgap energy on these parameters, especially film thickness and applied potential, has been investigated recently in electrodeposited ZnO films. Marotti *et al.* [12] reported that bandgap energies vary inversely with film thickness

(1 μm – 30 μm), and increase with more negative deposition potentials. Pauportè *et al.* [29] found that the optical bandgap energy varies with electrolyte composition, applied potential, and post-deposition treatment. However, the fundamental reasons for these bandgap variances, especially with film thickness and deposition potential, have not yet been adequately explored. For example, there is only one recent study which attributes shifts in the absorption edge of electrodeposited ZnO films prepared at different temperatures to quantum confinement effects resulting from a large dispersion in crystallite sizes [32].

The main objective of this thesis is to study the fundamental reasons for the optical bandgap energy variation depending on film thickness, deposition potential, and sample aging time, to provide further guidance for optical property tuning in electrodeposited ZnO thin films. First in Chapter 2, theoretical basics for ZnO electrodeposition and bandgap energy are introduced. Chapter 3 talks about the preparation parameters and characterization methods for ZnO thin films. Phase-pure wurtzite ZnO identification and crystal morphology control are discussed in Chapter 4. Chapter 5 discusses the dependence of bandgap energy on film thickness, applied potential, and sample aging time in thin ZnO films (< 2 μm). Finally, Chapter 6 describes preliminary investigations to understand the influence of substrates, *in situ* Atomic Force Microscopy (AFM) of ZnO growth, and the effect of additives in the electrolyte.

The data that we present in this work suggest that factors other than quantum confinement are responsible for absorption edge shifts in our electrodeposited films.

This is the first study to investigate the hydrogen doping effect in electrodeposited ZnO, even though hydrogen is a well known *n*-type dopant in vapor deposited ZnO [33]. Further more, this thesis work is consistent with (and preceded) a very recent theoretical study that has shown that hydrogen donors are most likely trapped in local defect sites in ZnO crystals [34].

Chapter 2

Theory

One of the challenges in this thesis research was to find appropriate electrodeposition parameters to prepare ZnO thin films with uniform morphologies and repeatable optical properties. An understanding of the electrodeposition mechanism guided this parameter adjustment. In this Chapter, the proposed mechanism for ZnO electrodeposition is described in detail. For TFT applications, the channel layer material's bandgap energy is closely associated with its other properties such as channel mobility and carrier concentration, so the bandgap energy is critical for TFTs' performance. Reasons for variations in ZnO bandgap energies will be introduced in this Chapter for a better understanding of the bandgap discussion in Chapter 5.

2.1 Electrodeposition of ZnO

A mechanism for ZnO electrodeposition has been proposed by Switzer [35] and Izaki [23] as shown in Equations 2.1 and 2.2. Zn^{2+} ions form $Zn(OH)_2$ under basic

pH conditions, and $Zn(OH)_2$ is then converted to ZnO (at temperatures above 50 °C) [36]:

$$Zn^{2+} + 2OH^- \rightleftharpoons Zn(OH)_2. \tag{2.1}$$

$$Zn(OH)_2 \rightleftharpoons ZnO + H_2O. \tag{2.2}$$

Figure 2.1 shows a potential *vs.* pH (Pourbaix) diagram for stabilities of Zn ions and phases [37] based on thermodynamical calculations with Zn in the presence of water at 25 °C. The potential is given with respect to a Ag/AgCl reference electrode (E *vs.* Ag/AgCl). The potential/pH phase boundaries can shift if other ions are included in the solution or if the temperature changes. The black circle represents the initial potential and pH conditions used for ZnO electrodeposition in this thesis work. In the presence of an applied potential, the electrolyte undergoes electrochemical reactions to produce OH^- ions. Therefore, the electrolyte pH shifts to a higher value (the gray circle) and Zn^{2+} becomes $Zn(OH)_2$ as described in Equation 2.1. Since the $Zn(OH)_2$ phase is unstable at temperatures above 50 °C, it will be converted to ZnO as described in Equation 2.2.

2.1.1 Nitrate Reduction

Nitrate reduction is a common way of producing basic pH conditions in electrolytes [35]:

$$NO_3^- + H_2O + 2e^- \rightleftharpoons NO_2^- + 2OH^-. \tag{2.3}$$

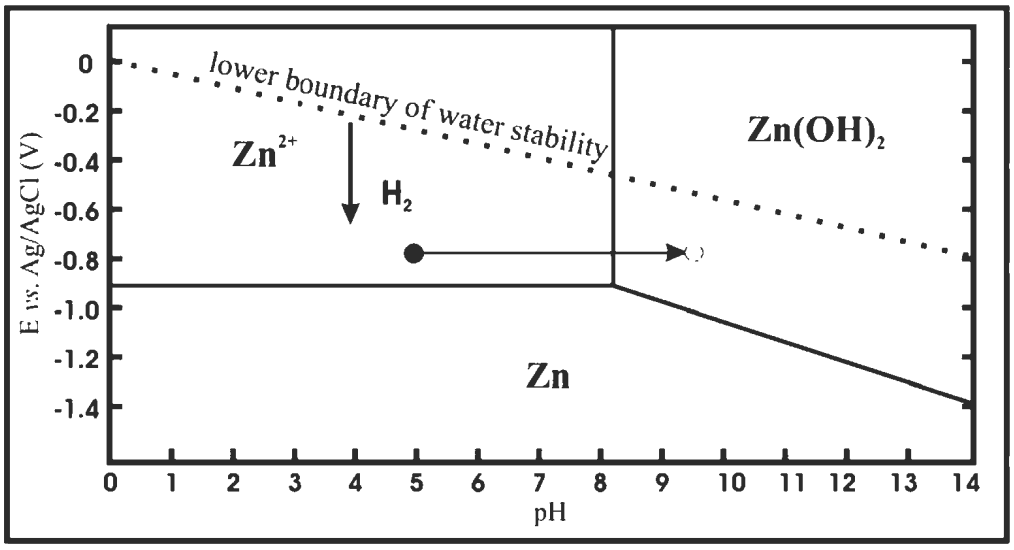

Figure 2.1: Pourbaix diagram for Zn ion and phase stabilities.

Thermodynamical calculations show that NO_3^- ions can be reduced to NO_2^- at potentials more negative than –0.197 V *vs.* Ag/AgCl in neutral pH electrolytes [38]. Therefore, in $Zn(NO_3)_2$ electrolytes, the global chemical reaction is

$$Zn^{2+} + NO_3^- + 2e^- \rightleftharpoons ZnO + NO_2^- \qquad E^0 = +0.289 \text{ V } vs. \text{ Ag/AgCl.} \tag{2.4}$$

The potential E^0 is calculated from the standard Gibbs free energies derived from each chemical species formation Gibbs free energy in the aqueous phase [39].

2.1.2 Oxygen Reduction

Oxygen reduction is another common way of producing basic pH conditions in electrolytes [36]:

$$O_2 + 2H_2O + 4e^- \rightleftharpoons 4OH^-. \tag{2.5}$$

Thermodynamical calculations show that O_2 can be reduced to produce OH^- at potentials more negative than +0.597 V *vs.* Ag/AgCl in neutral pH electrolytes [36].

In order to control the oxygen reduction rate, pure oxygen gas is normally bubbled into the electrolyte. Different concentrations of dissolved oxygen can result in different zinc oxide crystallite morphologies [40].

If another OH^- source is used, such as nitrate ions, it can be desirable to remove O_2 from the electrolyte for more controlled reaction conditions [38, 12]. Because argon is heavier than oxygen, ultrahigh pure argon purging can displace oxygen from the electrolyte. In order to expel all oxygen from the electrolyte, the purging rate is very critical. Slow purging will leave some oxygen in the electrolyte, while vigorous and turbulent purging will result in more oxygen being incorporated into the electrolyte from the air.

An optimal purging rate can be identified by monitoring for electrochemical oxygen reduction. Figure 2.2 shows cyclic voltammogram (CV) data wherein the current response was recorded as a potential was swept across a polycrystalline Au electrode in dilute H_2SO_4 at 50 mV/s. Changes in current indicate electrochemical reactions or absorption/desorption processes at the gold electrode and the peak area is related to the charge involved in the process. In this case, the broad anodic peak above +1.30 V is due to the oxidation of gold at the surface of the working electrode. The cathodic dip near +0.80 V is due to the reduction of the gold oxide back to gold metal. The areas of these two peaks are equal due to equal amounts of electron transfer for

the gold oxidation and reduction processes. If there is oxygen in the electrolyte, a cathodic oxygen reduction dip will also appear at more negative potentials, shown schematically here near –0.10 V. By adjusting to the optimal argon purging rate, there will be minimal oxygen left in the electrolyte, and the oxygen reduction dip will disappear and the CV curve will center at 0 mA/cm^2.

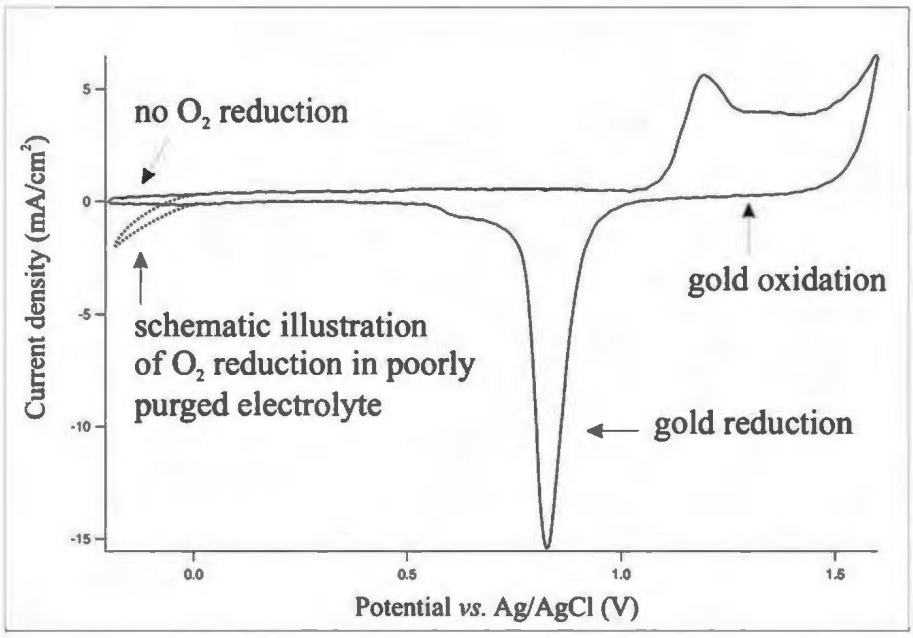

Figure 2.2: Cyclic voltammogram of gold oxidation and reduction reaction collected in dilute H_2SO_4, and a schematic illustration of the effect of oxygen in the electrolyte.

2.1.3 Hydrogen Evolution

Water electrolysis is a process by which water is converted to hydrogen and oxygen gas as shown in Equation 2.6:

$$2H_2O \rightleftharpoons 2H_2 + O_2. \tag{2.6}$$

The hydrogen evolution reaction and the oxygen evolution reaction do not happen at the same potential. Thermodynamic calculations show that hydrogen can be produced in aqueous electrolytes (pH = 5) at potentials more negative than –0.30 V *vs.* Ag/AgCl, and oxygen can be produced at potentials more positive than +0.90 V *vs.* Ag/AgCl [37]. In our experiments, hydrogen evolution can occur at the working electrode (where ZnO deposition occurs) and create a more basic pH environment (OH^-) as shown in Equation 2.7:

$$2H_2O + 2e^- \rightleftharpoons H_2 + 2OH^-. \tag{2.7}$$

Oxygen evolution can occur at the counter electrode, as shown in Equation 2.8:

$$2H_2O - 4e^- \rightleftharpoons O_2 + 4H^+. \tag{2.8}$$

In the Pourbaix diagram in Figure 2.1, the dotted line shows the lower boundary of water stability. Water is stable at pH and potential regions above this line, while hydrogen evolution will happen at pH and potential regions below this line. Because ZnO electrodeposition happens at pH and potential values at which water is not stable, there is hydrogen gas present in our electrodeposition environment.

2.1.4 Electrochemical Side Reactions

Electrochemical side reactions can also happen during the ZnO electrodeposition process. For example, electrochemical oxidation or corrosion can happen to some substrates, such as aluminum and steel, which can be detrimental to ZnO electrodeposi-

tion. Complementary reactions such as oxygen evolution can happen at the counter electrode and interfere with the electrodeposition at the working electrode. However, these problems can be avoided by using electrochemically stable substrates, such as stainless steel which is used in this thesis work, and by placing the working electrode and counter electrode far away from each other.

2.2 Bandgap Energy

A material's bandgap is defined as the energy gap between its valence band and its conduction band. Materials can be categorized into three classes by the magnitude of their bandgap energies: insulators (large bandgap), semiconductors (smaller bandgap), and conductors (no bandgap). Schematic illustrations of these three types of materials are shown in Figure 2.3.

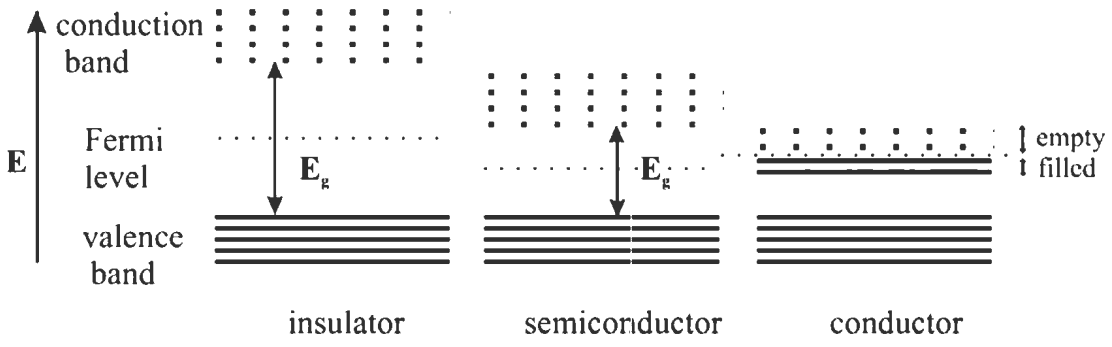

Figure 2.3: Schematic illustrations of bandgaps in insulators, semiconductors, and conductors.

The magnitude of a semiconductor's bandgap can be changed by dopants. A donor donates electrons to the conduction band and an acceptor accepts electrons

from the valence band. For example, in semiconducting Si, group VI elements like P act as donors while group III elements like Al act as acceptors. Semiconductors with mostly donors are n-type (negative type) and conduct mainly through electrons while semiconductors with mostly acceptors are p-type (positive type) and conduct mainly through holes.

A schematic illustration of how donors and acceptors change the bandgap energy is shown in Figure 2.4. An electron donor has an energy level close to the bottom of the conduction band. Electrons from this donor energy level can be thermally excited into the conduction band and contribute to the conduction. Therefore, when an electron in the valence band is excited, it first leaps to the donor energy level and then to the conduction band. In this way, the bandgap decreases to the energy difference between the top of the valence band and the donor energy level. An acceptor works in a similar way. An electron acceptor has an energy level close to the top of the valence band, so the bandgap decreases to the energy difference between the acceptor energy level and the bottom of the conduction band.

However, there are exceptions to this picture when a material's bandgap energy increases due to electron donors. According to the Moss-Burstein effect, donors can fill the conduction band and increase the bandgap energy. Burstein [41] explained this effect by taking into account the shapes and thus the effective states density of the conduction band and the valence band. Generally, in materials which show the Moss-Burstein effect, the conduction band has a sharp curvature (associated with

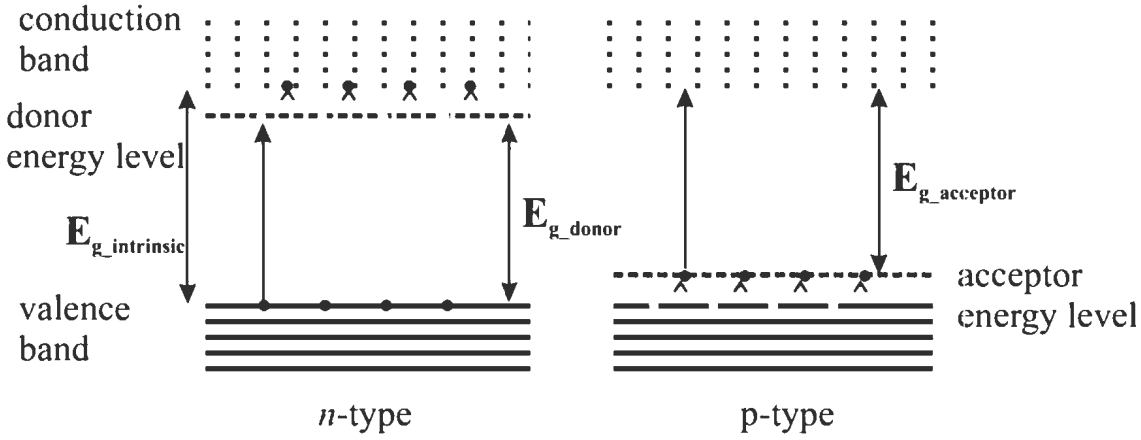

Figure 2.4: Schematic illustration of bandgap energy changes in n-type and p-type semiconductors.

small effective mass), and a small effective density of states and small degeneracy concentration ($1.2\times10^{17}/\text{cm}^3$ at 300 K for InSb). When heavily doped, a degenerate semiconductor's dopant band is very close to the bottom of the conduction band, and spreads into the conduction band as shown in Figure 2.5. Therefore, when electrons from the dopant band fill the conduction band, due to the low effective density of states at the bottom of the conduction band, the Fermi level increases drastically. The bandgap energy, from the top of the valence band to the lowest of unfilled level in the conduction band, is thus increased.

At present, it is still not possible to predicte in which semiconductors the Moss-Burstein effect will happen. However, the Moss-Burstein effect has been reported in semiconductors such as InSb [41], InN [42], and ZnO [43, 44], all of which are degenerate semiconductors and have sharp conduction band. In ZnO, the Moss-Burstein effect has been observed for dopants such as hydrogen [33, 45], aluminum [43], gallium

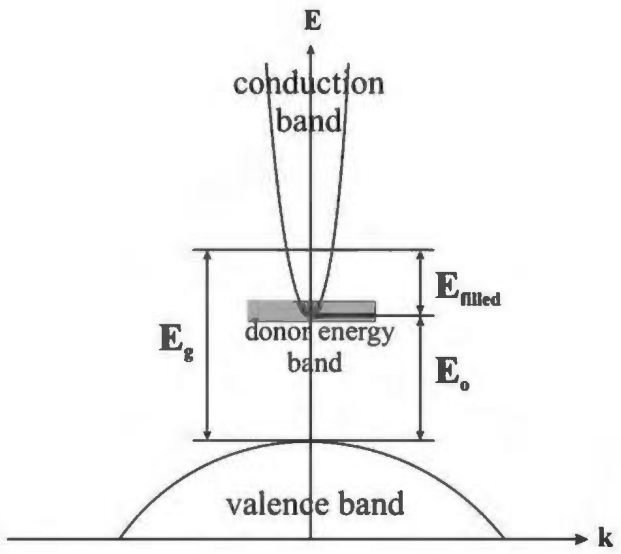

Figure 2.5: Schematic illustration of the Moss-Burstein effect.

[46] and indium [47]. For example, after ZnO:Al film deposition by magnetron co-sputtering, Oh *et al.* [33] annealed films in hydrogen gas. No significant change in the thin film crystallinity was found, but film resistivity decreased and optical bandgap energy increased for longer annealing times. These bandgap increase and resistivity decrease were attributed to the hydrogen doping which induced the Moss-Burstein effect. Since there exists hydrogen gas in our electrodeposition environment due to the voltage-induced hydrogen evolution, we have to consider the possibility of the hydrogen-induced Moss-Burstein effect in our electrodeposited ZnO thin films.

In addition to the doping examples described above and mentioned in Chapter 1, another possible reason for bandgap energy shifts could be electronic quantum confinement effects. Quantum confinement can happen for ZnO crystal sizes which are

comparable to the ZnO exciton radius (2 nm) [48]. For example, quantum confinement effects have been reported for ZnO crystal size close to 1 nm [48] and 20 nm [32]. Therefore, in our ZnO bandgap study, several possibilities will have to be considered to give a full picture of the fundamental reasons for the bandgap variance.

Chapter 3

Experiment

A material's properties are closely related to its preparation method and parameters. Based on the electrodeposition mechanism described in Chapter 2, we identified deposition parameters such as electrolyte composition, substrate, purging rate, and temperature as important parameters to deposit morphologically uniform ZnO thin films. A variety of characterization methods were used to interpret information on crystalline phases, crystal orientations, deposit morphologies, film thicknesses, optical bandgap energies, and crystal defect concentrations. These methods are outlined in this Chapter.

3.1 Synthesis

3.1.1 Equipment

Our conventional three-electrode electrochemical cell, as shown in Figure 3.1, is a practical adaptation of a traditional setup described by Bard and Faulkner [49]. This setup was used for all ZnO electrodepositions described in this thesis. It is comprised of three electrodes: a working electrode (WE), a reference electrode (RE), and a counter electrode (CE). The RE (Ag/AgCl in this thesis work) is a close approximation to a non-polarizable electrode whose potential is not changed by small amounts of current flow. The RE provides a reference for comparing the WE potential. The WE is where electrodeposition occurs. When a potential is applied between the WE and the RE, a current flows through the WE as ZnO forms at the WE surface. The third electrode, the counter (auxiliary) electrode, is where complimentary chemistry occurs to connect and balance the aqueous circuit. The CE is a gold wire (2.1 mm diameter) and is placed far away from the WE to separate the two chemistry sites as much as possible.

The three electrodes are connected to a potentiostat (Hokuto Denko HA-501) to keep a constant potential in the range of –0.90 V to –1.50 V between the WE and the RE by adjusting the current at the CE. During the process of electrodeposition, the charge passed between the WE and the CE can be collected by a coulomb/amperehour meter (Hokuto Denko HF-201). The current-voltage data is recorded and analyzed

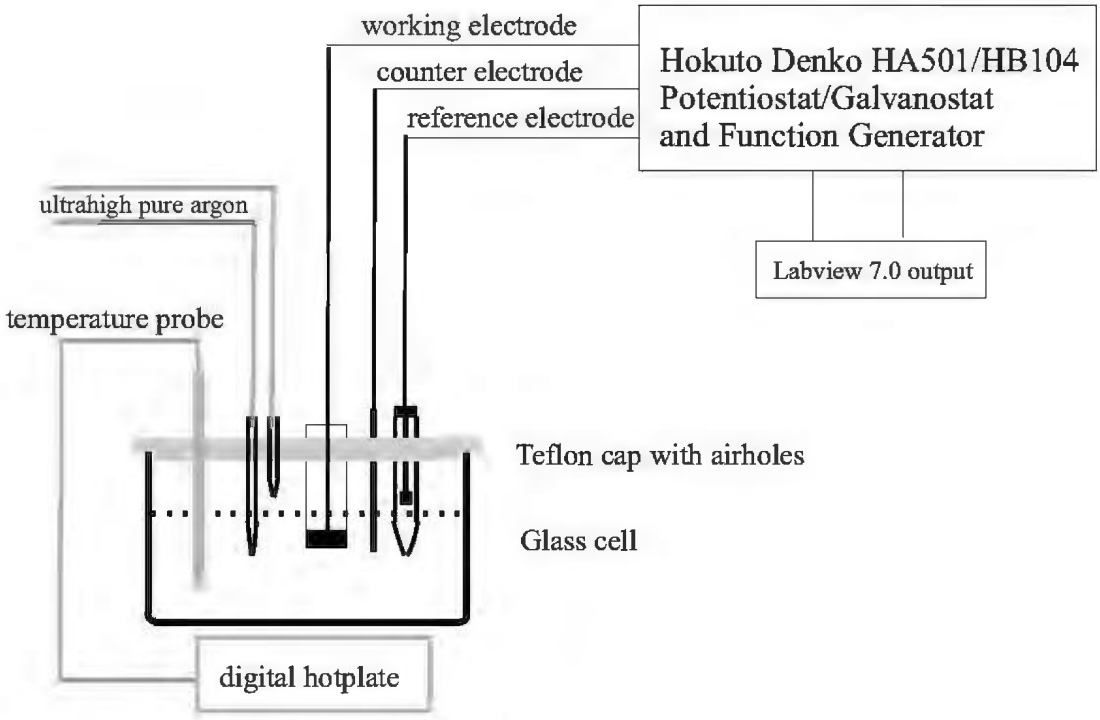

Figure 3.1: Schematic diagram of the ZnO electrodeposition setup used in this thesis work.

using LabVIEW 7.0 (National Instruments) virtual instruments, some of our own design and others modified from D. Bizzotto *et al.* [50].

3.1.2 Electrodeposition Procedure

We synthesized ZnO using the method first reported by Izaki and Omi [23]. The electrolytes commonly used for ZnO electrodeposition involve zinc salts, such as $Zn(NO_3)_2$ [23] or $ZnCl_2$ [51], dissolved in water. The concentration of Zn^{2+} is normally between 0.05 M and 0.10 M [25, 38]. In our experiments, 0.01 M $Zn(NO_3)_2$ electrolyte was used to produce relatively slower ZnO crystal growth rate than higher concentration $Zn(NO_3)_2$ electrolytes. All electrolytes were prepared from ACS reagent grade salts (EM Scientific) and ultrapure water (Barnstead Nanopure, 18.2 MΩ·cm).

A Fisher Scientific Isotemp digital hotplate and temperature probe were used to maintain a constant electrolyte temperature at 70 °C. Ultrahigh purity argon gas (minimum purity 99.999%) was purged into the electrolyte to remove oxygen. Two argon purge tubes were used to seal the oxygen out of the electrolyte: one tube below the liquid level the other above the liquid level. The WE was connected to the potentiostat by a polycrystalline brass mask, and was secured using a Teflon head and a glass cylinder. The substrate (WE) was cut from a stainless steel sheet (0.10 mm thickness) with a deposition area of 38 mm^2. It was pretreated by sanding with 1500 grit sand paper (grit size: 12.6 μm) to remove the contaminants from the surface and sonicating for five minutes in ultrapure water to dislodge any remaining grit. We note

that the sand paper grit size is an order of magnitude larger than our electrodeposited ZnO crystallite size.

In preparation for deposition, the RE and the CE were dipped into the 0.01 M $Zn(NO_3)_2$ electrolyte and connected to the potentiostat. The electrochemical cell was then heated to 70 °C, and argon gas was purged into the electrolyte. A constant potential was applied between the WE and the RE before the WE reached the electrolyte to ensure continuous potential control throughout the deposition process.

3.2 Characterization

3.2.1 X-Ray Diffraction

Phase identification and crystal orientation information were obtained through X-ray diffractometry (XRD) using a Rigaku RAC-C diffractometer. The principle for XRD is Bragg's law,

$$n\lambda = 2d\sin\theta, \tag{3.1}$$

where λ is the incident X-ray wavelength, n refers to the nth constructive interference, d is the d-spacing between the crystal planes, and θ is the angle between the incident X-rays and the sample surface.

Bragg's law is illustrated in Figure 3.2. Incident X-rays are reflected by electrons from a set of crystal planes. The scattered beams can constructively interfere when the pathlength difference ($2dsin\theta$) is an integer multiple of the wavelength. In our

experiments, first order constructive interference was used ($n = 1$), incident $Cu\ K\alpha$ X-ray wavelength is fixed (1.54056 Å), and ZnO crystal d-spacing has different discrete values along different crystal orientations. As shown in Figure 3.3, the sample rotates relative to the incident light while the detector rotates twice as fast as the sample. Therefore, when the angle between the sample plane and the incident X-ray beam (θ) satisfies Bragg's law with different d-spacing values during the sample rotation process, there will be constructive interference and thus the Bragg peaks.

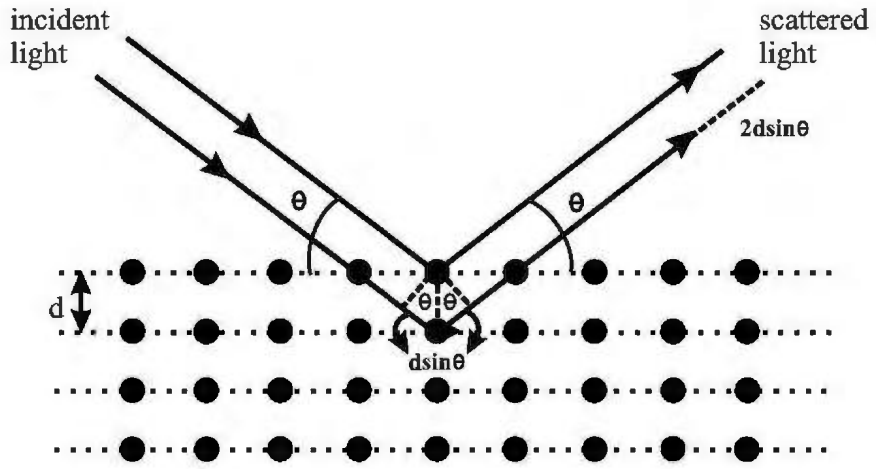

Figure 3.2: Schematic illustration of Bragg's law.

The Joint Committee for Powder Diffraction Studies (JCPDS) has filed a standard wurtzite ZnO XRD pattern (JCPDS #36-1451) [52], as shown in Table 3.1 and Figure 3.4, which was obtained from packed randomly oriented powders.

In our experiments, qualitative phase identification was performed by visually comparing the peak positions of the measured XRD patterns to the standard pat-

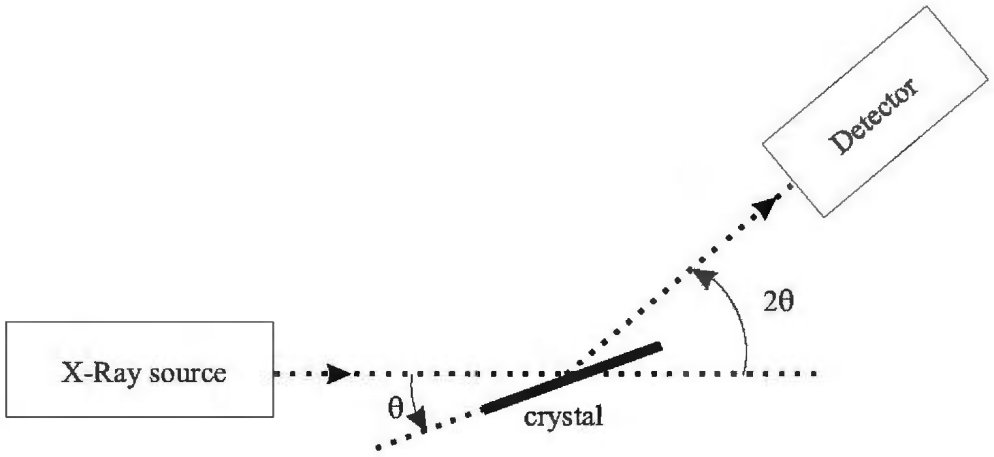

Figure 3.3: Schematic illustration of an X-ray diffractometer.

2θ	(h k l)	Intensity
31.770	1 0 0	57
34.422	0 0 2	44
36.253	1 0 1	100
47.539	1 0 2	23
56.603	1 1 0	32
62.864	1 0 3	29
66.380	2 0 0	4
67.963	1 1 2	23
69.100	2 0 1	11

Table 3.1: Standard XRD pattern for wurtzite zinc oxide, JCPDS #36-1451. The peak intensity is given relative to the largest peak (002).

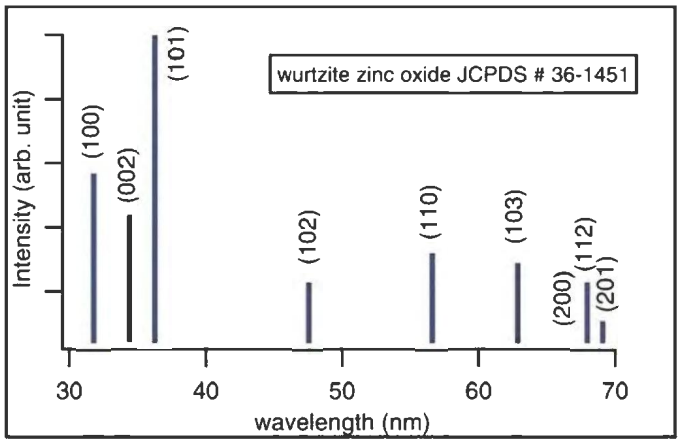

Figure 3.4: Standard XRD pattern for wurtzite zinc oxide (JCPDS #36-1451).

tern. Next, quantitative identification required the sample's lattice constants to be compared with the standard wurtzite ZnO lattice constants. The lattice constants are associated with the interplanar spacing (d_{hkl}). Equation 3.2 defines the interplane spacing for hexagonal crystal structures:

$$\frac{1}{d^2} = \frac{4}{3}\left(\frac{h^2 + hk + k^2}{a^2}\right) + \frac{l^2}{c^2}, \tag{3.2}$$

where d_{hkl} is associated with the Bragg peak positions (2θ) as shown in Equation 3.1. Given the observed Bragg peak positions, their *hkl* indexes, and the crystal class, a material's lattice constants can be obtained. However, due to systematic errors in XRD measurements, such as sample displacement and curvature of the sample plane, which both create errors in the angle between X-ray and the sample plane, a 2θ angle correction is needed for the Bragg peak positions before determining the lattice constants. LATCON [53], a sub-program of PROSZKI designed by D. Schwarzenbach *et al.* [54], uses a least square method to refine the best value for 2θ zero shift correction

and the lattice constants based on the observed Bragg peak positions and the crystal class. After the 2θ correction, the modified Bragg peak positions can be used to re-calculate lattice constant values. In order to determine initial peak positions, XRD patterns were processed by several procedures which are listed in the Appendix 1.

Preferred orientations of crystallites in a material were assessed by comparing the relative peak intensities with a standard powder pattern. The average crystallite size of the sample can be obtained by using the half intensity peak width as shown in Scherrer formula [55],

$$t = \frac{0.9\lambda}{B cos\theta_B}. \tag{3.3}$$

Here, t is the average crystallite size, λ is the incident X-ray wavelength, B is the peak width (2θ in rad) at half peak intensity, and θ_B is the peak position (θ). The bigger the average crystallite size is, the sharper the Bragg peak will be.

3.2.2 Scanning Electron Microscopy

Top-view and cross-sectional images of ZnO films can be obtained from Scanning Electron Microscopy (SEM). In this thesis, a Hitachi S570 SEM was used to image our ZnO thin films.

The SEM requires a high vacuum for operation [56]. An electron gun emits a beam of high energy electrons from the electron source. This electron beam travels downward through a series of magnetic lenses and is focused to a fine spot about 10 nm. At the same time, the potential between the electron gun cathode and anode at the bot-

tom of the SEM accelerates the electrons with high velocity. Near the bottom, a set of scanning coils moves the electron beam to look at different spots on the sample. As the electron beam hits the sample, photons and electrons are knocked off, including primary backscattered electrons, secondary electrons, cathodoluminescence, X-ray, and Auger electrons. The primary backscattered electrons provide atomic number and morphological information, secondary electrons provide morphological information, cathodoluminescence provides electrical information, X-ray provides compositional information throughout thickness, and Auger electrons provide surface sensitive compositional information. In our experiments, secondary electrons were used to generate images of ZnO deposits.

SEM images show crystal morphology information, but direct interpretation of morphology based on colour contrast is not wise. The contrast in an SEM image is related to electron interactions with the crystals. The more conductive the sample is and the higher atomic numbers of the atoms in it, the brighter it will appear in the SEM images. In addition, taller crystallites which have stronger interactions with the electron beam will appear brighter. Figure 3.5 is an SEM image of an electrodeposited ZnO thin film. The hexagonal crystal pillars are scattered on the stainless steel substrate. Because those crystallites are taller than the substrate, crystallites appear brighter and the substrate appears darker. Our substrates were sanded in the same directions as the rolling lines. The size of background corrugation ($\sim$ 1 μm) is smaller than the sand paper grit size ($\sim$ 12 μm), so the background

corrugation is likely due to the rolling lines native to the substrates. The length scale at the right lower corner is 1.20 μm, so the ZnO crystal size is about 200 nm.

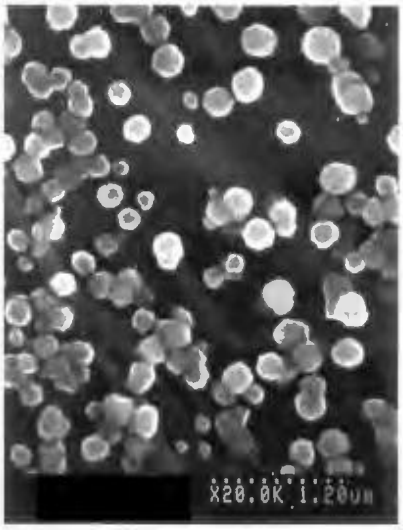

Figure 3.5: An SEM image of an electrodeposited ZnO thin film on a stainless steel substrate.

SEM images show clear top-view crystal morphologies, but are not as clear for the cross-sections. The relatively small film thickness (< 1 μm) makes it hard to observe the boundary of the substrate and the ZnO deposit. Therefore SEM cross-section measurements are not generally accurate for our film thickness determination.

3.2.3 Atomic Force Microscopy

Atomic Force Microscopy (AFM) is also used to image our electrodeposited samples. The advantage of AFM is that it can measure real sample heights for conductive or non-conductive samples, and it can be used in liquid or in ambient conditions. An Asylum Research MFP-3D AFM was used in this thesis work.

A schematic illustration of how an AFM works is shown in Figure 3.6. An AFM images surface topographies based on tip-sample interactions such as Van der Waals forces. The cantilever is normally Si with a resonant frequency on the 10 – 100 KHz scale. In this thesis work, the cantilever oscillates with a resonant frequency $\sim$ 300 KHz and driving amplitude near 1.00 V. When the cantilever tip interacts with the sample, perturbing forces cause an amplitude decrease. A laser beam is directed onto the back of the cantilever. It is deflected and then detected by the AFM feedback system. Based on the deflected laser beam position, the feedback system adjusts the AFM cantilever base height to maintain a constant tip oscillation amplitude. This cantilever base height was rapidly adjusted during the AFM scan and so it follows the change in height of surface features.

There could be artifacts in AFM images of crystallite topography due to tip-sample convolution. For example, a rectangular object, when measured with a similarly dimensioned AFM tip (diameter $\sim$ 10 nm), can have a trapezoidal AFM cross-section with a side slope close to that of the tip angle. These artifacts made it hard to image the top-view of our zinc oxide crystallites ($\sim$ 100 nm). However, film thickness can be measured using AFM large scale scans. ZnO samples were partly scraped to leave a clean cut between the ZnO deposit and substrate. Figure 3.7 shows the optical view of an AFM scan at the deposit-substrate boundary taken by the AFM optical camera. Figure 3.8 is the top-view AFM image showing the ZnO deposit area and clean substrate area. A clear vertical step was seen in the cross-section image and

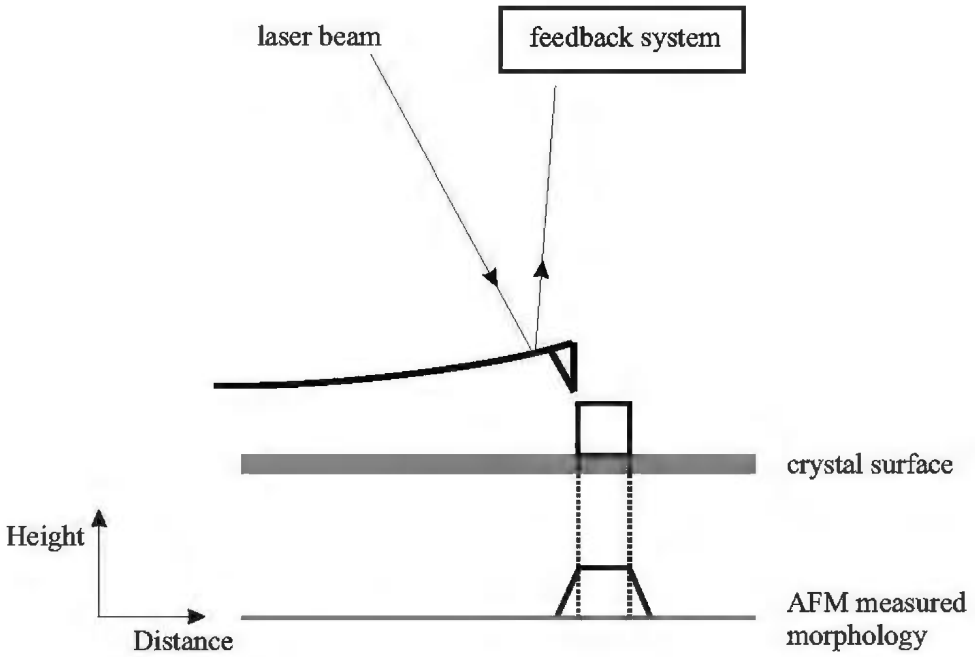

Figure 3.6: Schematic illustration of how an AFM works.

it corresponds to the boundary of deposit and substrate. The average film thickness for this ZnO deposit is 600 nm. The uncertainty for the measurement is 200 nm due to variation in deposit roughness. AFM was also used for the *in situ* electrochemical studies as well, which is discussed in Chapter 6.

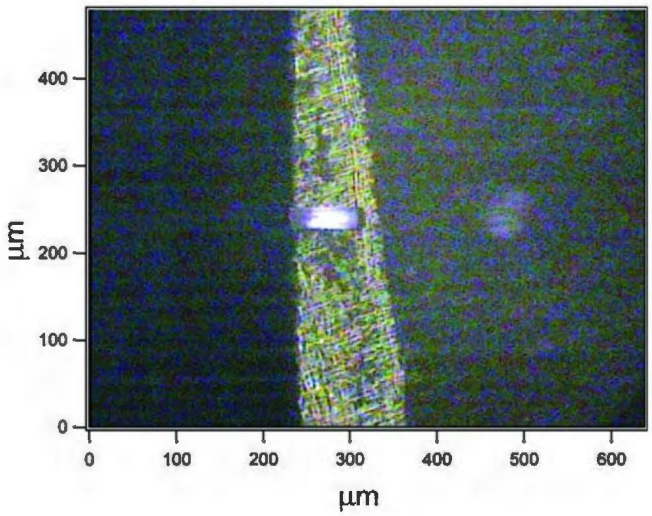

Figure 3.7: AFM optical view of the edge of a zinc oxide sample. The left dark part is the cantilever, the middle bright part is the substrate, and the right dark part is the ZnO deposit. The AFM cantilever has a laser spot on its back.

3.2.4 Raman Spectroscopy

Raman modes can be used to interpret ZnO film characteristics such as preferred orientation [57], crystal defect/doping level [58, 59], and crystal mechanical stress [57, 60] through Raman peak positions and their relative intensities.

When light is incident on a material, elastic or inelastic scattering can happen. In elastic scattering, also called Rayleigh scattering, the incident photon energy remains

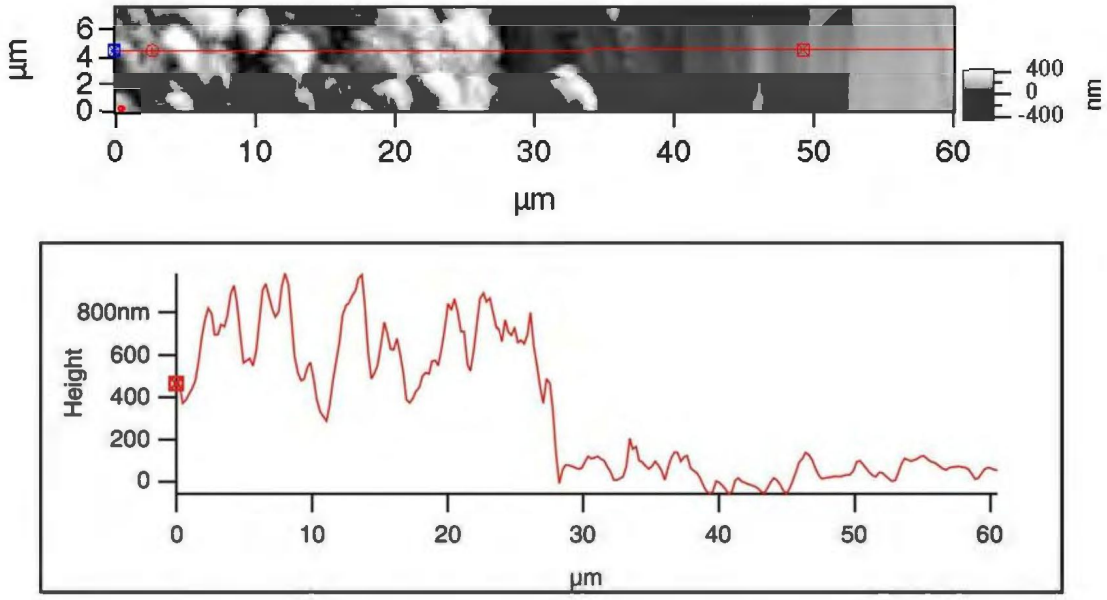

Figure 3.8: A large scale AFM image and the height cross-sectional information used for a film thickness measurement.

unchanged. For inelastic scattering, Stokes and anti-Stokes transitions can happen (Figure 3.9). Electrons can be excited to a higher virtual level, which has an energy much lower than an electronic quantum level ($\sim$ eV), and has a very short lifetime ($\sim 10^{-14}$ s). Therefore, excited electrons soon radiate back to a lower vibrational level and release photons. This vibrational level still has a higher energy than the original ground energy state and so the radiated photon has a smaller energy than the incident photon. The energy difference between the incident photon and radiated photon becomes the crystal lattice vibration. This energy shift is expressed by the wavenumber ($1/\lambda$) shift as shown in Equation 3.4,

$$\nu = 1/\lambda_{incident} - 1/\lambda_{scattered}, \tag{3.4}$$

where the $\lambda_{incident}$ and $\lambda_{scattered}$ are the wavelength of the incident and the scattered photons, respectively. This is the Stokes effect (normal Raman scattering) [61] and is used in Raman spectroscopy. The anti-Stokes effect has a scattered light energy larger than the incident light energy.

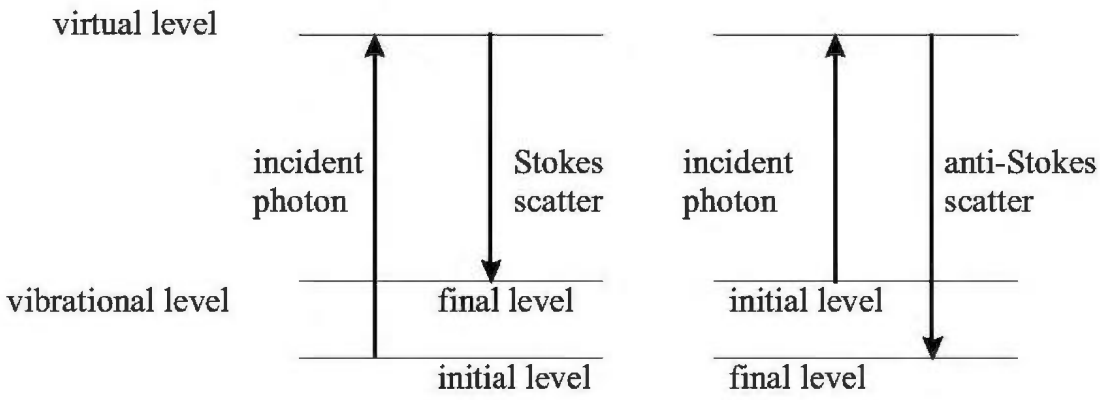

Figure 3.9: Schematic illustration of the Stokes effect and the anti-Stokes effect.

In Raman experiments, the incident light electric field (**E**) can change the polarizability (α) of the crystal and induce an electric dipole moment (**P**) in the sample as shown in Equation 3.5,

$$\mathbf{P} = \alpha \mathbf{E}. \tag{3.5}$$

Raman selection rules require a dipole moment change after the excitation of the incident light [61]. Therefore, the Raman effect happens when a crystal's polarizability can be changed by the incident light electric field. In similar measurements with Infrared Spectroscopy (IR), infrared selection rules require a permanent electronic dipole in the first place. Therefore, Raman is useful for IR inactive substances, such

as H_2 and N_2. For our ZnO investigations in air, IR spectra show strong H_2O peaks which cover up the characteristic ZnO peaks. Raman spectroscopy is not as sensitive to H_2O molecules because O-H has a very small electronic dipole change after the photon excitation. Therefore, Raman spectroscopy is very suitable for ZnO studies in air.

Raman Spectroscopy (LabRAM, Jobin Yvon Horiba, 532 nm) experiments described in this thesis were done in a backscattering geometry with confocal collection lensing. The scattered light is detected from the same direction of the incident light that is normal to the substrate plane, with two beam splitters before reaching the spectrometer. Figure 3.10 shows the schematic illustration of the Raman spectroscope used in this thesis work.

Common phonon modes for wurtzite ZnO structure include both polar modes and non-polar modes. Polar modes have longitudinal optical modes (LO) and transverse optical modes (TO) which are split into different lattice symmetries, A1 and E1. In addition to the polar modes, there are two non-polar modes with E2 symmetry. The E2 (low) mode is associated with the heavy zinc sublattice vibration while the E2 (high) mode is associated with the oxygen sublattice vibration [62]. The modes with footnote 1 are polar modes while modes with footnote 2 are non-polar modes. Table 3.2 shows the common phonon mode frequencies for bulk wurtzite zinc oxide [63].

These Raman modes have been used to interpret ZnO crystal information. For example, Cong *et al.* [57] reported that the intensities of the A1 (TO) and E2 (high)

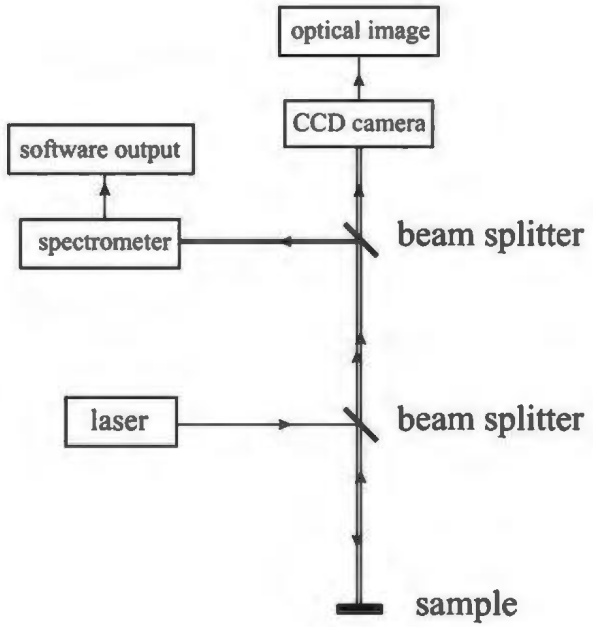

Figure 3.10: Schematic illustration of a Raman spectroscope.

Raman mode	Frequency(cm^{-1})
E2 (low)	101
E2 (high)	437
E1 (TO)	407
E1 (LO)	583
A1 (TO)	381
A1 (LO)	574

Table 3.2: Frequency and symmetry of the fundamental phonon modes in bulk wurtzite zinc oxide.

phonon modes were enhanced with the increase in ZnO (002) XRD peak intensity. They attribute the phonon mode intensity enhancements to the improvement of ZnO crystal quality along (002) orientation. Reuss *et al.* [59] reported that the intensity of the E1 (LO) phonon mode was inversely proportional to the annealing temperature for Ga- or N-doped ZnO thin films and bulk crystals. Therefore, the E1 (LO) phonon mode was attributed to the overall concentration of crystal defects, but not specifically to particular defect type.

3.2.5 UV-Vis Spectroscopy

Bandgap energies can be measured by methods such as cathodoluminescence, photoluminescence, and Ultraviolet-Visible (UV-Vis) spectroscopy. Two common UV-Vis spectroscopy modes are transmittance mode and reflectance mode. Transmittance mode provides optical bandgap energy and transparency information, but it requires transparent substrates or self-supporting materials. Reflectance mode provides only bandgap energy information. In this thesis, diffuse reflectance (DRS) spectroscopy was used for our electrodeposited ZnO thin films because they were supported by opaque stainless steel substrates.

The UV-Vis diffuse reflectance spectroscopy set-up is illustrated in Figure 3.11. A UV-Vis source (180 nm – 800 nm) angled at 45° to the substrate plane illuminates the sample (OceanOptic DT 1000 CE spectrophotometer). When the UV-Vis light hits the sample, part of the light spectrum is absorbed by the sample to excite electrons

from the valence band to the conduction band, while the remaining part is reflected diffusely. The diffuse reflected light is collected by a spectrometer and output with respect to the incident light intensity (%). The maximum diffuse reflection standard is a white polymer (Spectralon, Ocean Optics). The minimum diffuse reflectance level is set by dark current in the absence of the UV-Vis light source. In other studies, substrates have been used for background substraction [22]. However, due to the relative smooth surface, there is no diffuse reflectance signal from our stainless steel substrates.

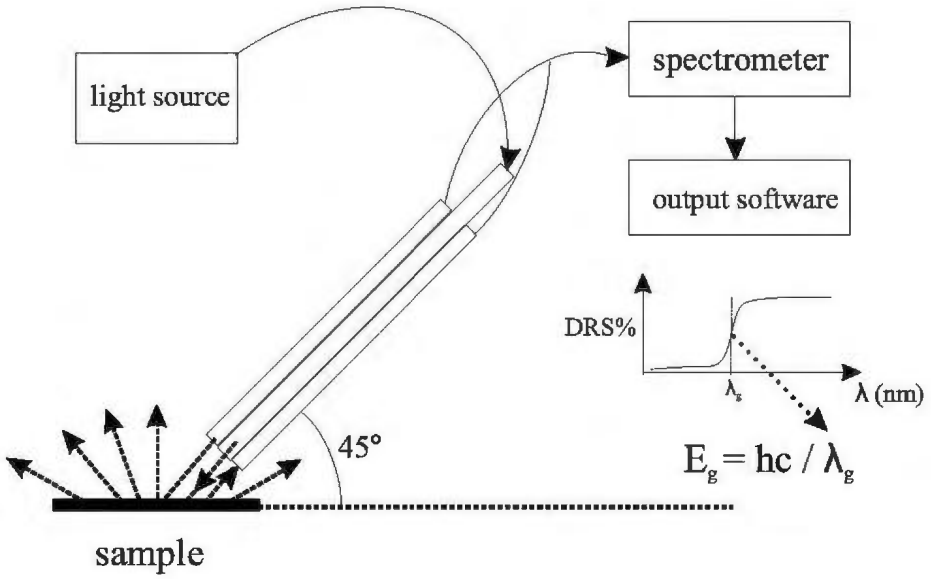

Figure 3.11: Schematic illustration of UV-Vis diffuse reflectance spectroscopy.

The bandgap energy (E_g) determination from diffuse reflectance spectra can be obtained through the first derivative of DRS signal. If the sample has a uniform crystal morphology and quality, the diffuse reflectance spectrum will be a vertical

transition with infinite slope at the absorption edge (λ_g). Therefore, d DRS/ $d\lambda$ goes to infinity at λ_g. However, due to defects and size variations among crystallites, the absorption edge extends into an absorption band. The bandgap wavelength (λ_g) is chosen to be the peak position of the first derivative of DRS [64] as shown in Figure 3.12. In this way, the wavelength near the middle of the transition is selected as λ_g to accommodate the variation of crystal quality. This λ_g is used to determine the bandgap energy,

$$E_g = hc/\lambda_g, \tag{3.6}$$

where h is Planck's constant and c is the speed of light.

On the other hand, from UV-Vis transmittance spectra, the optical bandgap energy can be obtained from a $(-ln(T)*h\nu)^2$ *vs.* $h\nu$ plot [12]. T is the transmittance which has the exponential form $e^{-\alpha}$, where α is the absorption coefficient. Therefore,

$$(-ln(T) * h\nu)^2 = (\alpha * h\nu)^2 = h\nu - E_g, \tag{3.7}$$

when $(-ln(T)*h\nu)^2$=0, the onset energy ($h\nu$) is used for the optical bandgap energy. It has been reported that this method leads to bandgap energies that are 0.10 eV higher than the first derivative (DRS) method [12]. In addition, this transmittance method leads to underestimation of bandgap energy for small crystallites [31]. Therefore, the first derivative method is used in this thesis work for the optical bandgap energy measurement.

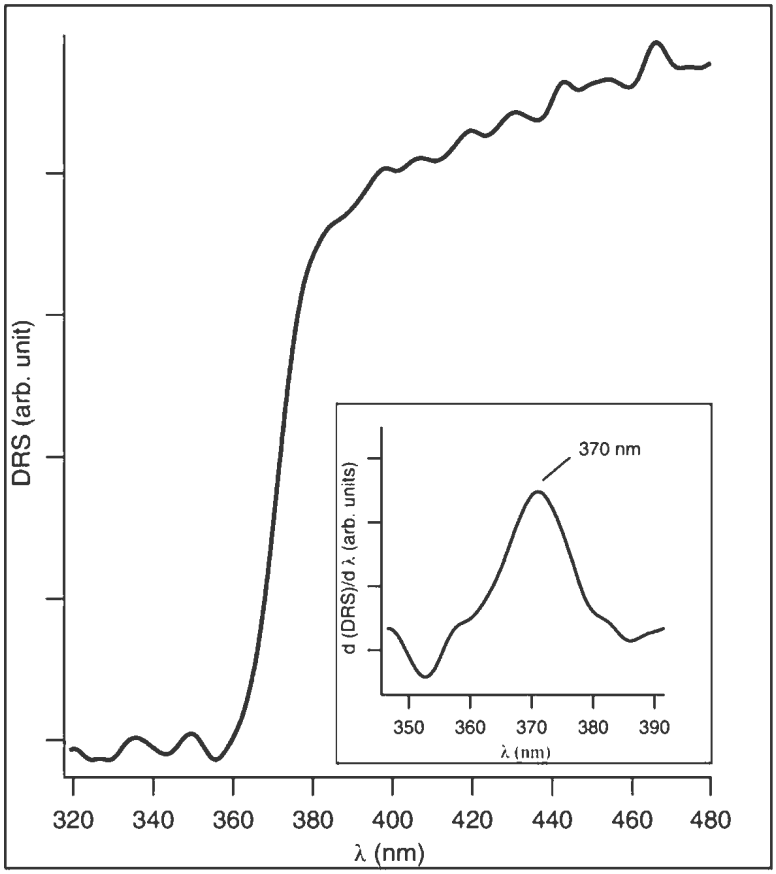

Figure 3.12: Representative UV-Vis diffuse reflectance spectrum (DRS) and first derivative of DRS for an electrodeposited ZnO thin film.

Chapter 4

Morphology and Size Control of Wurtzite ZnO Crystallites

Uniform crystal morphology and size lay the groundwork for uniform optical properties in thin film materials. In order to study crystal formation trends, this Chapter discusses the influence of electrodeposition parameters such as applied potential and film thickness on ZnO crystal morphologies, sizes, and crystal growth.

4.1 Phase Identification

Making phase-pure wurtzite ZnO was the first step for our morphology and optical property studies. We electrodeposited thin films potentiostatically from 0.01 M $Zn(NO_3)_2$ electrolytes at 70 °C on stainless steel substrates with ultrahigh purity argon gas purging throughout the process. Films were deposited at constant applied potentials between –0.40 V and –1.50 V. There was barely any deposit for samples

prepared at potentials more positive than –0.80 V. Film growth rates were higher at more negative potentials. Due to hydrogen evolution at the WE, films electrodeposited at potentials more negative than –1.10 V tend to have many visible pinholes, while films prepared at more positive potentials have visually uniform deposits.

The primary method of phase identification for these deposits is to determine lattice constants from XRD data and see if they are consistent with the wurtzite ZnO standard lattice constants. Three XRD patterns in the 2θ range between 30° and 70° are shown in Figure 4.1 as representative of deposits prepared at potentials between –0.90 V and –1.50 V. The total charge that flowed through the WE during a electrodeposition, relating to the number of electrons transferred in each chemical reaction occurring at the WE, was measured using a Coulumb meter. Bragg peaks in these patterns were compared with stainless steel (substrate), aluminum (sample holder), and the wurtzite ZnO (JCPDS #36-1451) standard patterns. The substrate and sample holder XRD peaks do not overlap with wurtzite ZnO standard peaks. Five to seven ZnO peaks were fit with Gaussian functions to obtain positional information, and these data were used for lattice constant refinements with the software package PROSZKI [54]. Figure 4.2(a) shows the refined lattice constants for thin films electrodeposited in the potential range –0.90 V to –1.50 V (film thickness: 500 nm – 2 μm). The unstrained ZnO crystal lattice constants are a=3.250 Å and c=5.207 Å as indicated by the horizontal lines in Figure 4.2. The lattice constants were calculated using three to five electrodeposited thin films at each potential (–0.90 V to –1.20 V);

for lattice constant calculations at potentials between –1.30 V to –1.50 V, each data point represents one sample. The lattice constants for most samples are within two estimated standard deviations of the unstrained wurtzite ZnO values.

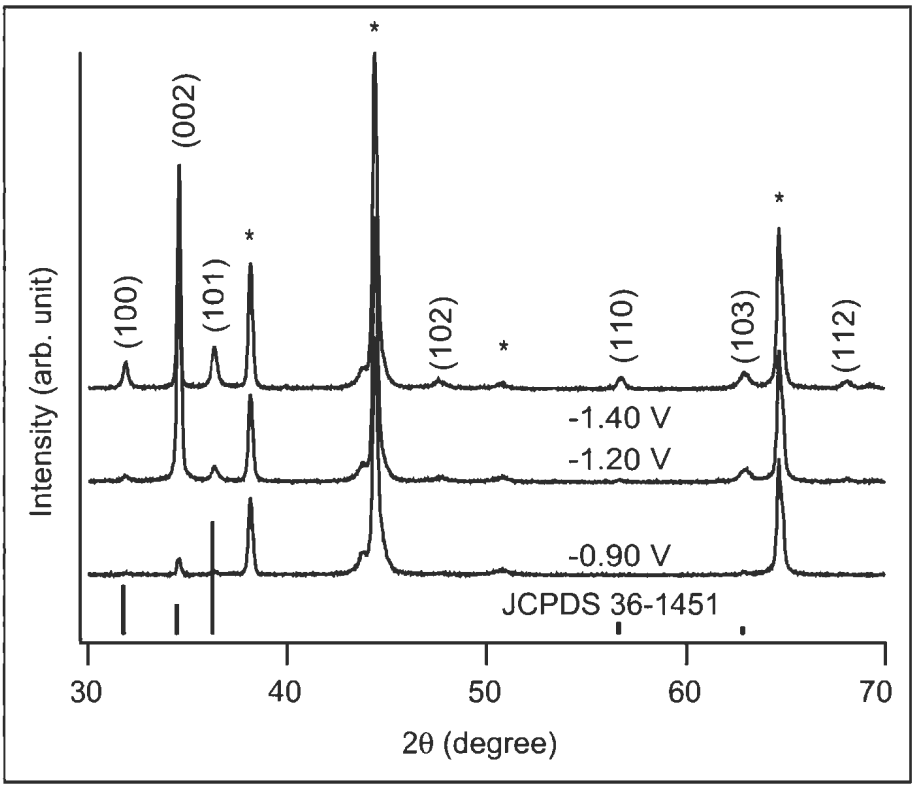

Figure 4.1: XRD data for thin films electrodeposited at different applied potentials (charge passed during the deposition given in parentheses): –1.00 V (0.25 C), –1.20 V (0.42 C), and –1.40 V (0.53 C). Peaks belonging to the stainless steel substrate and the aluminum sample holder are marked with asterisks (*).

Figure 4.2(b) shows the refined lattice constants for thin films electrodeposited at the same potential (–1.20 V) with different thicknesses. Every data point represents one sample. The trend of lattice constant change with film thickness is not clear in this graph, but variation is 0.006 Å. However, other studies have shown changes in lattice

constants with deposition conditions. For example, Marotti *et al.* [12] reported, for electrodeposited ZnO with different thickness ($\leq$ 5 μm), lattice constants can change up to 0.02 Å which they attribute to the presence of native defects. Pauportè *et al.* [29] reported similar lattice constant changes, which they explained by dopant incorporation in ZnO electrodeposits.

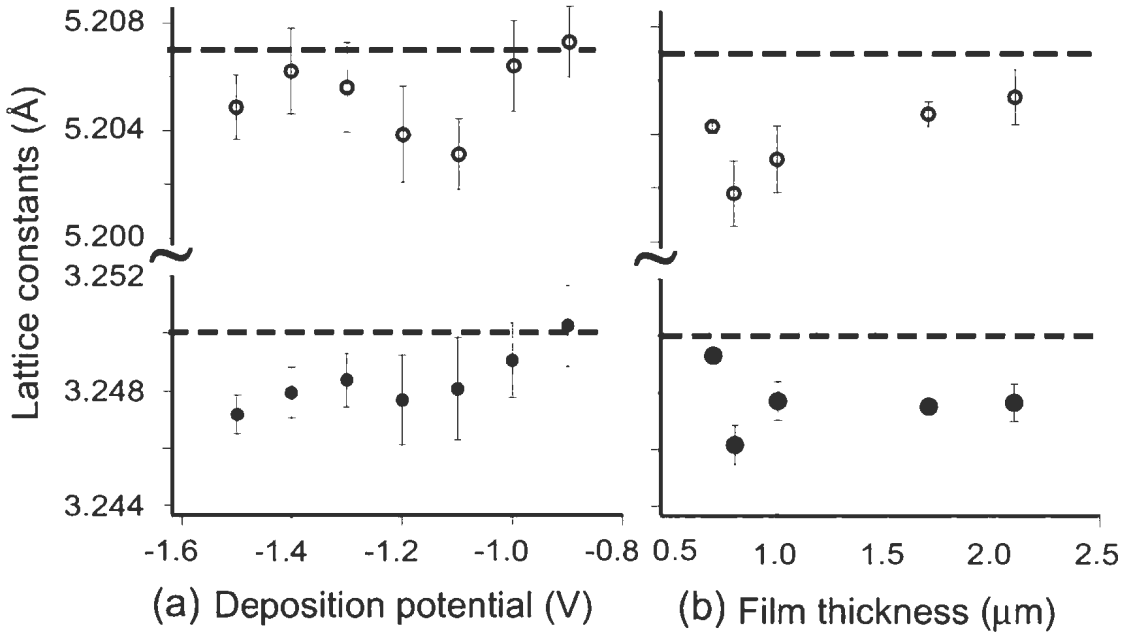

Figure 4.2: Lattice constants for ZnO thin films electrodeposited (a) at different deposition potentials and (b) at the same deposition potential (−1.20 V) with different film thicknesses. The unstrained ZnO crystal lattice constants are a=3.250 Å and c=5.207 Å as indicated by the horizontal lines.

4.2 Morphology and Size Tuning of ZnO Crystallites

Figure 4.3 shows how the total charge passed through the WE during ZnO electrodeposition varies as a function of deposition time. Each data point is an average value from one to three samples. The charge passed increases with increasing deposition time, showing a constant electrochemical reaction rate at each deposition potential.

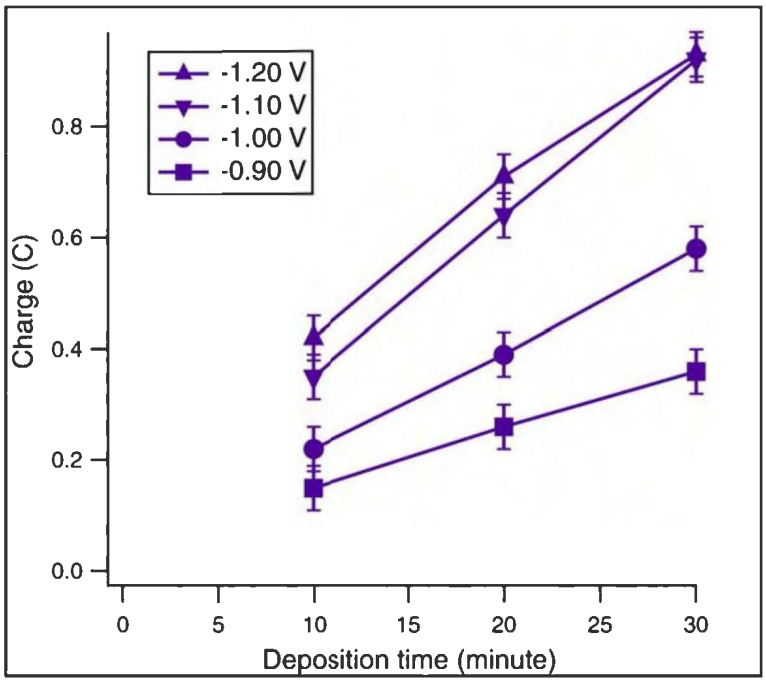

Figure 4.3: Charge passed during ZnO electrodeposition, as a function of deposition time, at different deposition potentials.

Figure 4.4 shows the trend in the ZnO film thickness as a function of charge passed during the course of electrodeposition. The film thicknesses were measured using AFM height measurements as described in Chapter 3. Each data point is an average of three to five thickness measurements on different spots of the sample.

Our electrodeposited ZnO film thickness is proportional to the charge passed during deposition for all applied potentials. Moreover, for a fixed amount of charge passed, the ZnO film thickness tends to increase with more negative potentials, indicating higher deposition rates at more negative potentials.

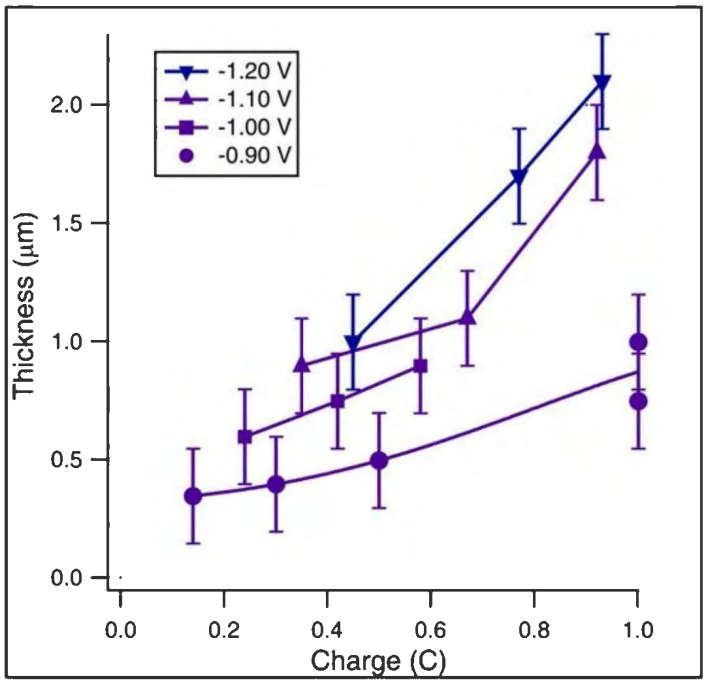

Figure 4.4: ZnO film thickness as a function of charge passed during electrodeposition for four different applied potentials.

The slopes of thickness *vs.* charge curves are different with potentials. One possible explanation for the differences is the difference in crystal compactness (film density). In order to measure crystal compactness, surface coverage analysis were attempted using an automated image processing routine developed by Muhammad Jehangir (M.Sc. student with Dr. Erika Merschrod, MUN Chemistry). The brighter objects in SEM images, corresponding to ZnO crystallites, were selected and their areas were

used to calculate the deposit coverage ratio. However, due to the crystallite height variance, it was hard to differentiate crystallites from substrates and results of these analysis were not satisfactory.

Crystal compactness was also examined with SEM cross section images. Figure 4.5 (a) shows the SEM cross-section image of a ZnO thin film prepared at –0.90 V with 500 nm thickness. It shows an open structure crystal morphology at –0.90 V. Figure 4.5 (b) is the SEM cross-section image of a ZnO thin film prepared at –1.20 V peeled from the substrate. It shows more compact crystallite growth with fewer voids.

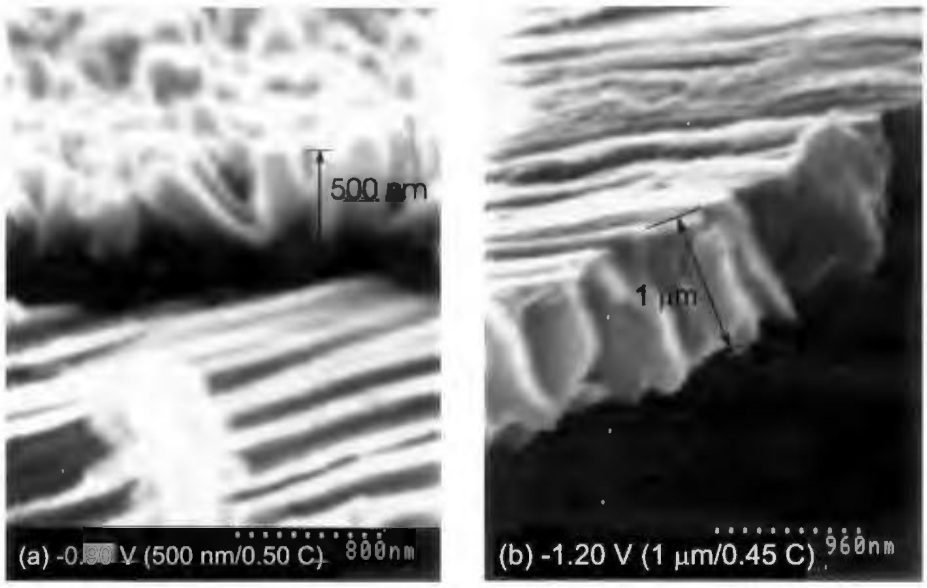

Figure 4.5: SEM cross-section images for ZnO thin films electrodeposited at (a) –0.90 V and (b) –1.20 V. The film thickness and charge passed during electrodeposition are noted in the images.

4.2.1 Morphology Control with Applied Potential

A change in growth mode with applied potential was found for ZnO electrodeposits. SEM images for three thin films with similar thicknesses (900 nm $\pm$ 200 nm), but electrodeposited at different potentials, are shown in Figure 4.6. A clear crystal morphology transition is shown between –1.00 V and –1.20 V. At more positive potentials ($E_{applied} \geq$ –1.10 V), hexagonal rod growth was observed. XRD data confirmed dominant growth of the *c*-axis perpendicular to the substrate plane. At more negative potentials ($E_{applied} \leq$ –1.20 V), "twin-rice" structures were observed, and the more negative the electrodeposition potential, the more close-packed the twin-rice structures tended to grow. In typical commercial ZnO varistor ceramics grown by the other methods, a twin-rice crystal structure has also been observed, with a $(000\bar{1})$-$(000\bar{1})$ crystal orientation (*c*-axis) along the long axis of the twin-rice structure and parallel to the substrate plane [65]. However, this crystallite morphology has not yet been reported for electrodeposited ZnO.

We have confirmed that this potential-dependent growth mode transition holds for ZnO electrodeposits on stainless steel and regular steel substrates, and also for electrodeposits in 0.01 M to 0.05 M $Zn(NO_3)_2$ electrolytes. The hexagonal rod to twin-rice transition was also observed at –1.10 V for ZnO electrodeposits on regular steel substrates in 0.01 M $Zn(NO_3)_2$ electrolytes, while the morphology boundary potential for ZnO electrodeposits on regular steel substrates in 0.05 M $Zn(NO_3)_2$ electrolytes is slightly more positive (–0.90 V).

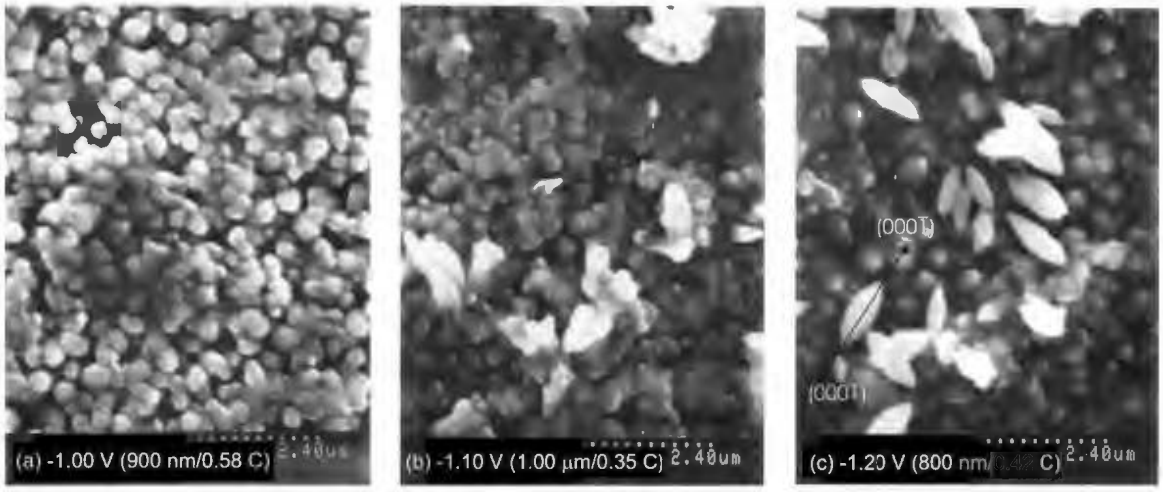

Figure 4.6: SEM images of ZnO thin films electrodeposited at different applied potentials (a) –1.00 V, (b) –1.10 V, and (c) –1.20 V. The film thickness and charge passed during electrodeposition are shown in the images.

Although the reason behind this morphology transition dependence on applied potential and electrolyte concentration is not clear, one possible reason is the change in ZnO electrodeposition rate. Izaki and Omi [19, 23] have reported that the ZnO deposition rate increases with more negative deposition potentials (–0.70 V to –1.40 V) and with higher $Zn(NO_3)_2$ concentrations (10^{-2} M to 10^{-1} M). In this thesis work, as shown in Figure 4.4, the ZnO deposition rate is higher for more negative potentials. Because the twin-rice crystal growth was associated with either more negative potentials or higher $Zn(NO_3)_2$ concentrations in our research, it is plausible that the twin-rice crystal growth is favored for a higher electrodeposition rate.

4.2.2 Size Control with Deposition Time

Figure 4.7 shows representative SEM images of ZnO thin films electrodeposited at fixed potentials with different thicknesses by changing deposition time. Deposits prepared at –0.90 V show hexagonal rods, and XRD data confirm the *c*-axis is perpendicular to the substrate plane. Crystallites increase in diameter for more charge passed (Figure 4.7(a–c)). For ZnO thin films electrodeposited at –1.20 V, the length and width of twin-rice crystallites increase for more charge passed (Figure 4.7(d–f)).

In order to quantitatively analyze the crystal size trend with the film thickness, average crystallite sizes (t) were calculated from Bragg peak widths and positions using the Scherrer formula as described in Chapter 3. Table 4.1 shows average crystallite sizes calculated from three main Bragg peaks for ZnO films. Due to low signal to noise ratio in some Bragg peaks, not all peaks are listed for all thicknesses. The measured peak widths at half maxima (FWHM) (B_m) have been modified by the instrumental broadening (B_s) for the corrected FWHM (B) as shown in Equation 4.1 [22].

$$B = \sqrt{B_m^2 - B_s^2} \tag{4.1}$$

However, due to standard silicon sample's average crystal size is unknown, the silicon sample's smallest FWHM was used as the instrumental broadening (0.00160 rad). To provide the best range of uncertainty, the crystal sizes reported in Table 4.1 are the average of the none broadening-corrected and broadening-corrected crystal sizes, and

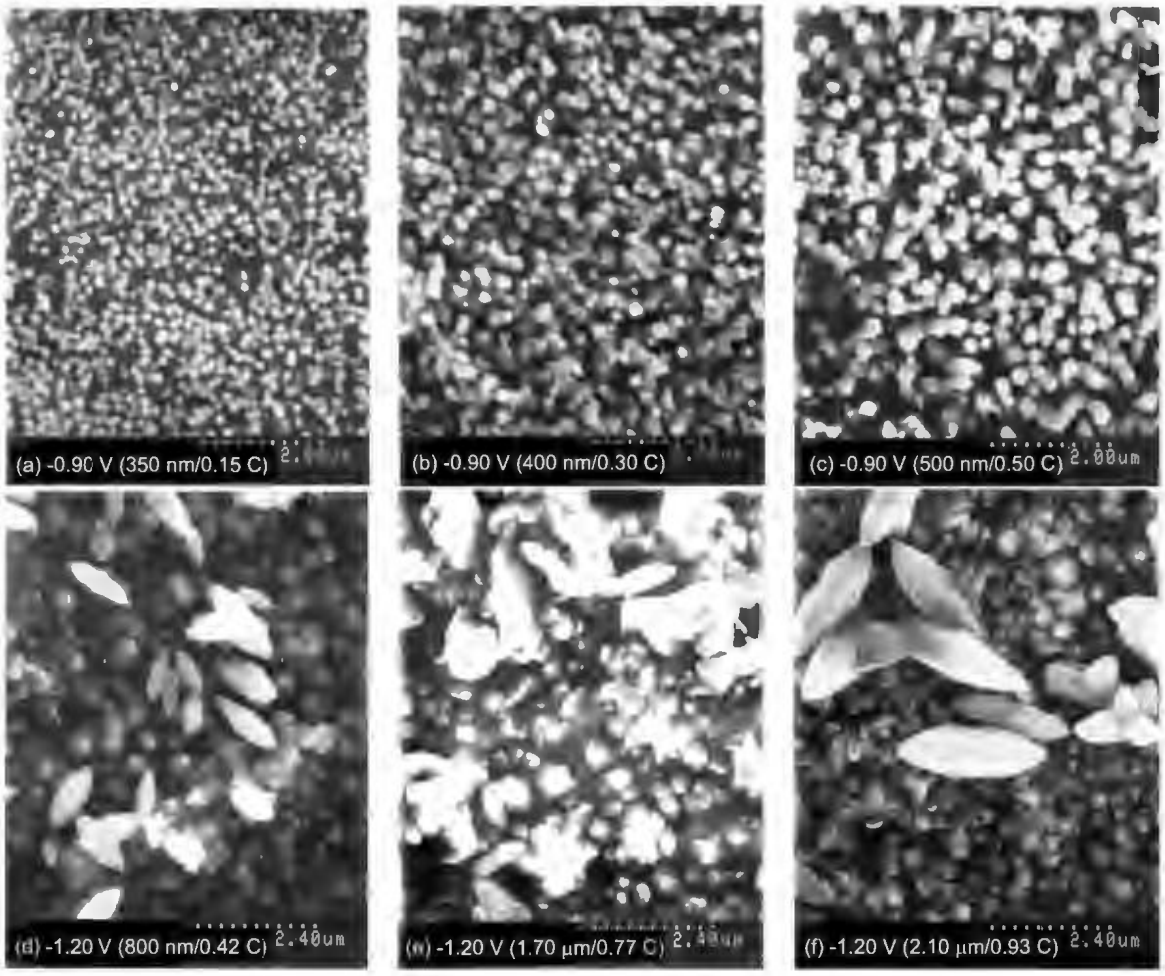

Figure 4.7: SEM images of ZnO thin films deposited at applied potentials (a-c) –0.90 V, and (d-f) –1.20 V. The film thickness and charge passed during electrodeposition are shown on the images.

the error was chosen as the half difference between the uncorrected and corrected values.

The calculated crystallite sizes are an order of magnitude smaller than the film thickness and the observed crystallite sizes from the SEM images in Figure 4.7. However, these calculated crystallite size data represent an average over the entire sample, including small crystallites which are not distinctly visible from the top-view SEM images. In addition, our crystallite size data are very close to that reported for electrodeposited ZnO prepared with similar parameters [22, 32].

As a general trend, the crystallite size along (002) direction (t_{002}) is larger than along the other two dimensions, which suggests an elongated crystal shape. However, there is no clear change in crystallite size with deposition potential or deposit thickness.

Deposition potential	Film thickness	t_{100}	t_{002}	t_{101}
−0.90 V	350 nm	–	89 ± 19 nm	43 ± 2 nm
	400 nm	42 ± 2 nm	96 ± 24 nm	59 ± 6 nm
	500 nm	50 ± 4 nm	100 ± 26 nm	54 ± 5 nm
−1.00 V	600 nm	44 ± 3 nm	96 ± 24 nm	39 ± 2 nm
	750 nm	48 ± 4 nm	98 ± 25 nm	43 ± 2 nm
	900 nm	48 ± 3 nm	94 ± 22 nm	46 ± 3 nm
−1.10 V	1000 nm	46 ± 3 nm	94 ± 22 nm	44 ± 3 nm
	1100 nm	39 ± 2 nm	99 ± 26 nm	38 ± 2 nm
	1800 nm	50 ± 4 nm	99 ± 26 nm	44 ± 3 nm
−1.20 V	800 nm	47 ± 3 nm	84 ± 17 nm	38 ± 2 nm
	1700 nm	47 ± 3 nm	89 ± 19 nm	39 ± 2 nm
	2100 nm	54 ± 5 nm	93 ± 22 nm	42 ± 2 nm

Table 4.1: Average crystallite sizes along different orientations for ZnO films with different thicknesses.

Chapter 5

Fundamental Studies of the Origin of the Tunable Bandgap Energy in Electrodeposited ZnO

ZnO bandgap energy is a critical factor in considering its performance as a material in TFTs because it is closely related to channel layer conductivity, carrier density, carrier mobility. Dopants such as Mg and Cd [27, 28] reduce ZnO's bandgap energy, as well as its conductivity, carrier density, and carrier mobility by donating electrons to the conduction band. However, in case of the Moss-Burstein effect [41], dopants such as Al [43], In [47], Ga [46], and H [33, 45] increase ZnO's bandgap energy, as well as conductivity, carrier density, and carrier mobility. Therefore, monitoring the bandgap energy provides important information relevant to ZnO performance as a channel layer material. This Chapter discusses several factors that influence the bandgap energy, such as film thickness, potential, and aging time, and the fundamental reasons behind these effects.

5.1 Bandgap Dependence with Film Thickness and Deposition Potential

Marotti *et al.* [12] have found that electrodeposited ZnO bandgap energy increases with film thickness (1 μm – 30 μm) and with more negative deposition potentials, for deposits prepared on copper substrates with 0.10 M $Zn(NO_3)_2$ electrolytes. However, other reports have shown that Zn^{2+} concentrations ($[Zn^{2+}]$) above 0.05 M tend to produce $Zn(OH)_2$ [36]. Consistent with this, Marotti *et al.* [12] have shown evidence of precipitated rather than electrodeposited ZnO at more negative potentials. To avoid the complications of precipitation reactions, this section describes studies to confirm the bandgap dependence in more dilute electrolytes (0.01 M $[Zn^{2+}]$) and for thinner films ($\leq$ 2 μm) relevant for TFT applications [3].

Optical bandgap energies of our electrodeposited ZnO were measured using UV-Vis diffuse reflectance spectroscopy (DRS). Figure 5.1 shows the DRS data for different thicknesses prepared at fixed potentials. Absorption edges of ZnO films shift to higher wavelengths (smaller bandgap energies) for thicker films. At potentials outside the –0.90 V to –1.20 V range, it is difficult to confirm either the bandgap energy or the film thickness. ZnO films prepared at potentials more positive than –0.90 V were too thin for thickness measurements, while films prepared at potentials more negative than –1.20 V have substantial variance in thicknesses at different spots on the sample. For films prepared in the –0.90 V to –1.20 V range, thicknesses are very

uniform (± 200 nm) and optical bandgap energies are very consistent at different spots on the sample.

The DRS data intensities depend primarily on the roughness of deposits, rather than the film thickness. For example, DRS intensities in Figure 5.1(a,b) decrease with film thickness, while DRS intensities in Figure 5.1(c) increase with film thickness. For films with the columnar morphology ($E_{applied} \geq -1.10$ V), roughness tends to decrease with film thickness as radial growth fills in more voids in the film, leading to more specular reflection and less diffuse reflection (Figure 5.1(a,b)). For deposition potentials which produce twin-rice crystallites ($E_{applied} \leq -1.10$ V), the films grow rougher with time, leading to less specular reflection and more diffuse reflection (Figure 5.1(c)). Therefore, the DRS intensity variance is directly related to different crystal morphologies for deposits prepared at different potentials.

Figure 5.2 shows how ZnO bandgap energies vary with deposit thickness at four different deposition potentials. The bandgap energy varies inversely with film thickness, at fixed potentials, for our electrodeposited ZnO. Moreover, for films of similar thickness, the bandgap energy increases as applied potential decreases from –0.90 V to –1.10 V, as shown in Figure 5.3. However, bandgap energies of –1.20 V deposits do not follow this trend. It is not clear why the bandgap energy of –1.20 V deposits are smaller than deposits at the other three potentials, but one possible reason could be related to the growth mode change (Figure 4.6) at more negative deposition potentials.

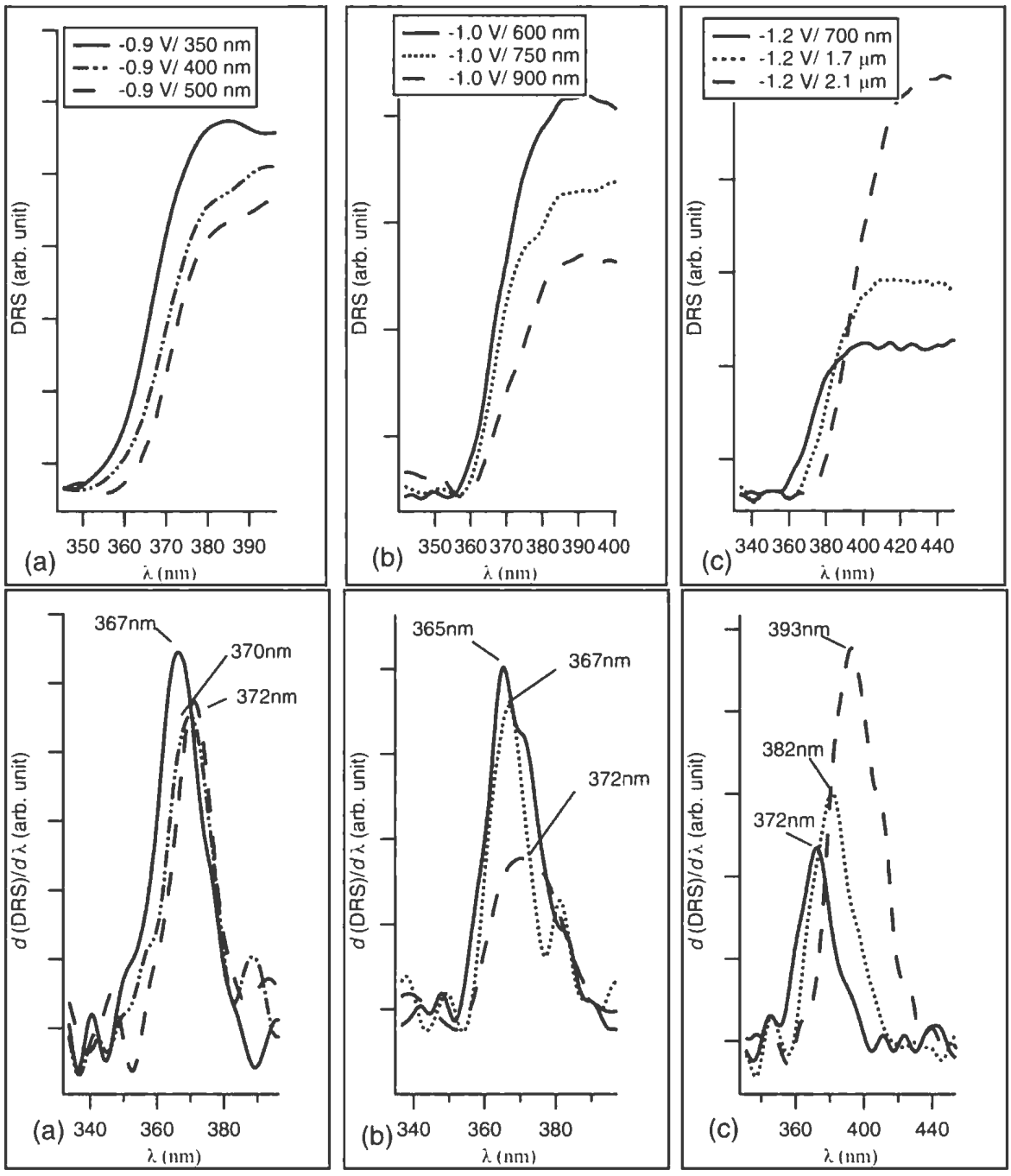

Figure 5.1: UV-Vis DRS spectra and first derivatives of DRS for ZnO thin films with different thicknesses electrodeposited at (a) –0.90 V, (b) –1.00 V, and (c) –1.20 V.

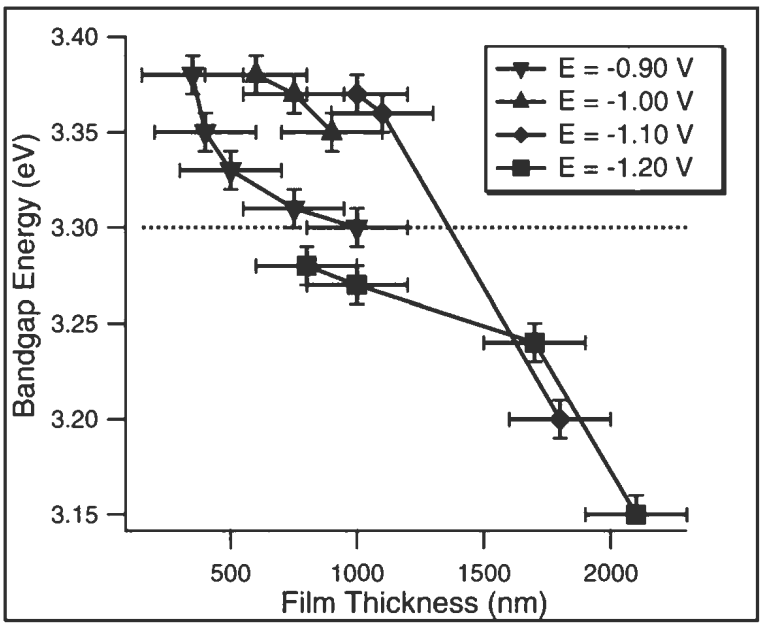

Figure 5.2: Optical bandgap energy as a function of film thickness for electrodeposited ZnO thin films. The dotted line indicates the bandgap energy for bulk wurtzite ZnO.

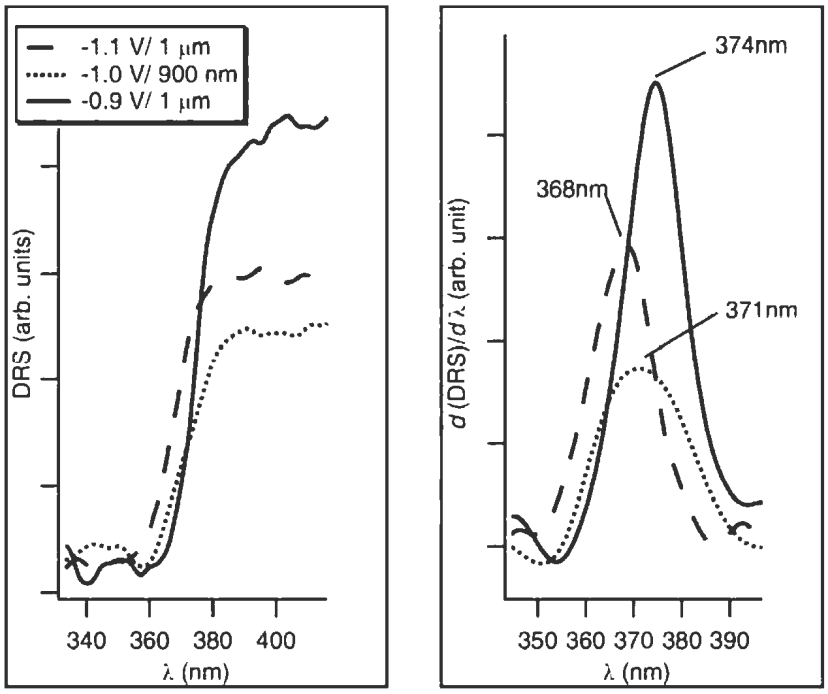

Figure 5.3: DRS spectra and first derivatives of DRS for ZnO thin films prepared at different potentials.

We achieved a 3.1 eV to 3.4 eV bandgap range using ZnO films ($\leq$ 2 μm). Marotti *et al.* [12] achieved a similar range in bandgap energy using much thicker electrodeposited ZnO films ($\leq$ 30 μm). The reasons that our deposits yielded a wide bandgap range using much thinner films are not immediately clear. However, possible explanations are explored and discussed in Section 5.3.

5.2 Bandgap Dependence with Aging Time

ZnO bandgap energies have been reported to vary with many factors such as film thickness [12], applied potential [12, 29], annealing time [33, 66], and crystal size [32, 67]. There have been few reports of optical bandgap changes with aging time [68], and no investigation of this effect in electrodeposited films [69]. Figure 5.4(a) shows UV-Vis DRS measurements for a fresh and aged ZnO thin film prepared at – 0.90 V (350 nm thickness). The absorption edge of the ZnO deposit shifts to a higher wavelength after days to weeks of aging in air. Figure 5.4(b) shows the bandgap change as a function of aging time for ZnO thin films prepared at different deposition potentials. Bandgap energies of ZnO thin films prepared at all the three potentials decrease after aging and stay constant after several weeks. The overall magnitude of the bandgap change ($\sim$ 0.05 eV) seems to be comparable for films prepared at different potentials and with different thicknesses.

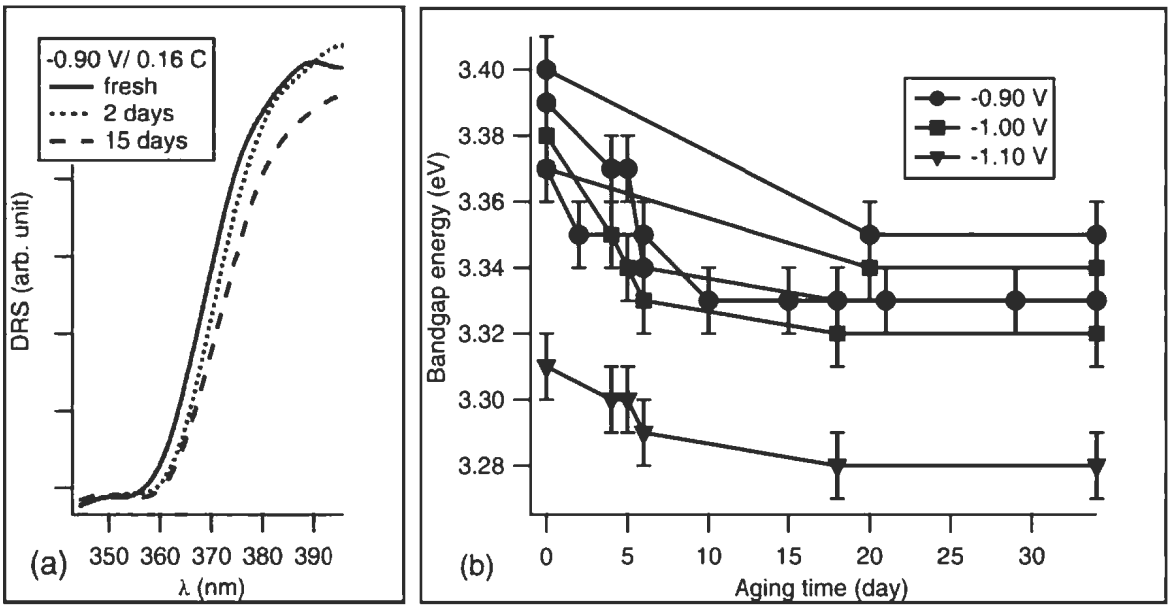

Figure 5.4: (a) UV-Vis DRS of a ZnO thin film in the process of aging and (b) the optical bandgap energy as a function of aging time for ZnO deposits prepared at different potentials.

5.3 Fundamental Reasons for Bandgap Energy Changes

Possible reasons for the bandgap energy dependences on film thickness, applied potential, and aging time could include quantum confinement effects [67, 32], mechanical stress [12], doping, or defects [47].

5.3.1 Quantum Confinement Effects

Optical quantum confinement of ZnO excitons, which have a Bohr radius ~ 2 nm [48], has been reported for ZnO particles from 1 nm to 60 nm [48, 32, 67]. The reported bandgap energies vary inversely with ZnO crystal sizes. For example, Wong *et al.* [67] achieved a bandgap energy range of 3.38 eV – 3.53 eV using electrophoretically

deposited nanoparticles of 2.1 nm – 2.7 nm. Marotti *et al.* [32] achieved a bandgap energy range 3.21 eV – 3.25 eV in electrodeposited ZnO with crystal sizes of 25 nm – 48 nm.

The bandgap energies of our electrodeposited ZnO as a function of average crystal size (along (100) direction (t_{100})) are shown in Figure 5.5. Bandgap energies of ZnO films prepared at potentials (–0.90 V to –1.10 V) are substantially higher than films prepared at –1.20 V, yet all have similar average crystallite sizes. Marotti *et al.* [32] reported that electrodeposited ZnO bandgap energies vary inversely with average crystal size, and that crystal size dispersion is also important. They report that 90% crystal size dispersion induces $\sim$ 0.005 eV bandgap energy increase for 45 – 50 nm average crystal size ZnO films. However, the bandgap energy differences we observe in films prepared at different potentials show much larger changes. This suggests that the crystal size dispersion effect does not affect the bandgap energy as much as the film thickness and the applied potential do. Therefore, quantum confinement effects are not the dominant reason for the bandgap energy changes in our electrodeposited ZnO films.

5.3.2 Mechanical Stress

Mechanical stress can be induced by dopants and defects, or it can also be the result of innate crystal growth stress or deposit-substrate stress. As shown in Figure 4.2(a,b), there is little variation in the lattice constants of ZnO deposits prepared at

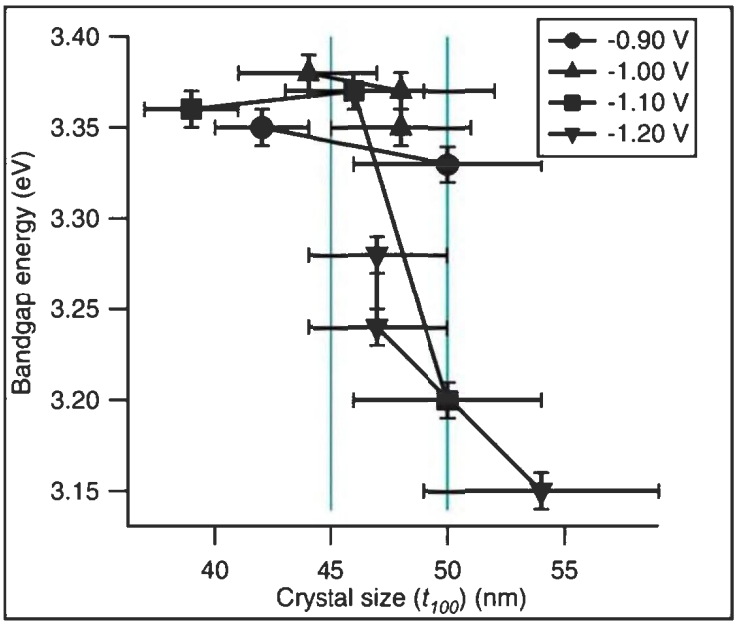

Figure 5.5: ZnO bandgap energy as a function of crystal size along the (100) direction.

different potentials, or for ZnO films prepared at the same potential with different thicknesses. All of the calculated lattice constants agree well with the standard lattice constant values of wurtzite ZnO. Raman spectra (discussed in Section 5.3.3) also show no evidence of stress, as the phonon mode peak position remain constant with changes in deposition potential and deposit thickness [57]. This evidence suggests that no substantial mechanical stress exists in our electrodeposited ZnO films.

5.3.3 Doping Effects

Dopants can also change ZnO's bandgap energy. Dopants such as Mg and Cd [27, 28] reduce the ZnO bandgap energy, while other dopants such as Al [43], In [47], Ga [46], H [33, 45] increase the ZnO bandgap energy due to the Moss-Burstein effect,

as described in Chapter 2. In our electrodeposition, nanopure water (18.2 MΩ·cm) and ACS reagent grade salts (impurity $\leq 0.001\%$) were used. Therefore, it is unlikely to have most of the impurities as mentioned above, except for hydrogen evolved from the aqueous electrolytes.

The hydrogen evolution rate, as described in Chapter 2, is closely associated with applied potential. Figure 5.6 shows the charge passed during electrodeposition at different potentials in 0.01 M $Zn(NO_3)_2$ electrolytes. We expect, in $Zn(NO_3)_2$, that the electron transfer reactions that contribute to the current are nitrate reduction and hydrogen evolution. It is possible that there is a small portion of the current due to minor reactions, but there is no electrochemical evidence of such reactions. If there is no Zn^{2+} and no NO_3^- in the electrolyte, such as in the KCl shown in Figure 5.6, hydrogen evolution is the dominant process. Therefore, the difference between the charge passed in $Zn(NO_3)_2$ electrolyte and KCl electrolyte can be attributed to the nitrate reduction, which leads to ZnO electrodeposition. Since more H_2 is evolved at more negative deposition potentials, it is possible that more hydrogen is also incorporated into ZnO thin films at these potentials.

There are many methods for hydrogen detection in ZnO, such as mass spectroscopy to monitor H_2 effusion, infrared spectroscopy [68], and Raman spectroscopy [58]. In Raman spectra, hydrogen local vibrational modes for atomic bonds (O-H, C-H, and N-H) have been reported in the range 2800 – 3200 cm^{-1} in bulk ZnO single crystal [70]. However, the same group could not find hydrogen modes in thin film ZnO.

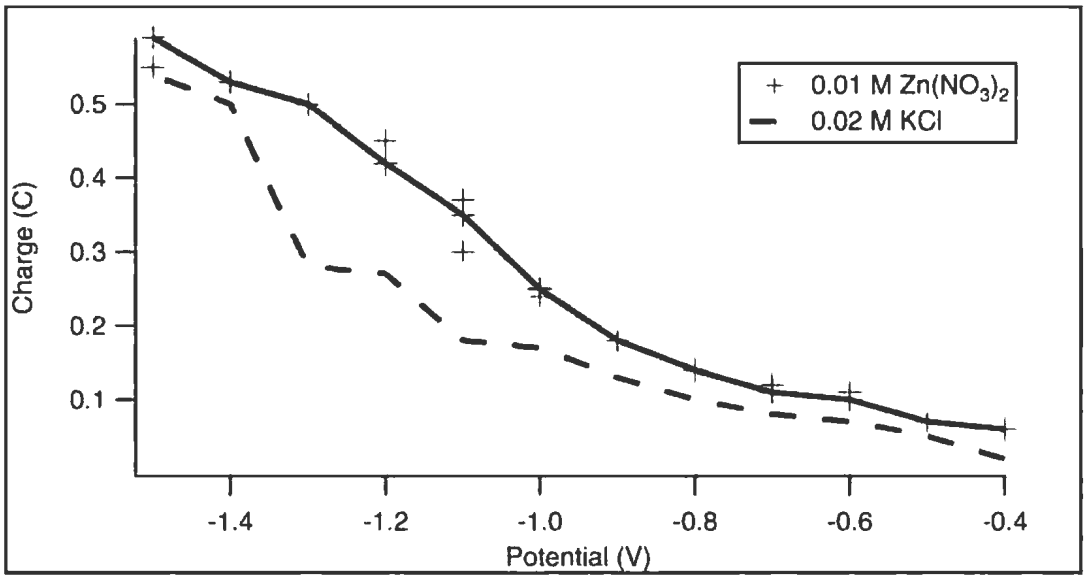

Figure 5.6: The charge passed during 10 minute of electrodeposition in 0.01 M $Zn(NO_3)_2$ and 0.02 M KCl.

Raman spectroscopy was performed on our electrodeposited ZnO films in search of hydrogen local vibrational modes (2800 – 3200 cm^{-1}). Figure 5.7 shows the Raman spectra comparison for ZnO deposits prepared at –0.90 V and –1.20 V, along with a spectrum of the substrate material (stainless steel). Due to the low signal to noise ratio, hydrogen local modes in our electrodeposited ZnO thin films were not readily detectable in all samples. There was no clear trend with deposition potential, film thickness, or aging time.

Intensities of Raman peaks in the 2800 – 3200 cm^{-1} region were increased dramatically after rinsing with ethanol and drying in air. Raman spectra of a ZnO film with and without ethanol rinsing are also shown in Figure 5.7, and the 2800 – 3000 cm^{-1} region shows significant increase after ethanol rinsing but with no substantial change

in peak positions. Since ethanol can change the surface termination of ZnO, it is not necessarily surprising that these light-mass modes are enhanced after an ethanol rinse. The peak fitting gives slightly different peak positions from the reported hydrogen local modes (C-H, C-H_2, and C-H_3) in bulk ZnO [70]. It is possible that this difference is due to different bonding environments for the hydrogen, especially at the crystallite surfaces. Quantum confinement effects for optical phonons [62] are less likely, since the shifts between our fitted peaks and the hydrogen local vibrational modes ($\sim$ 20 cm^{-1}) are an order of magnitude larger than the reported quantum confinement induced wavenumber shift ($\sim$ 2 cm^{-1}).

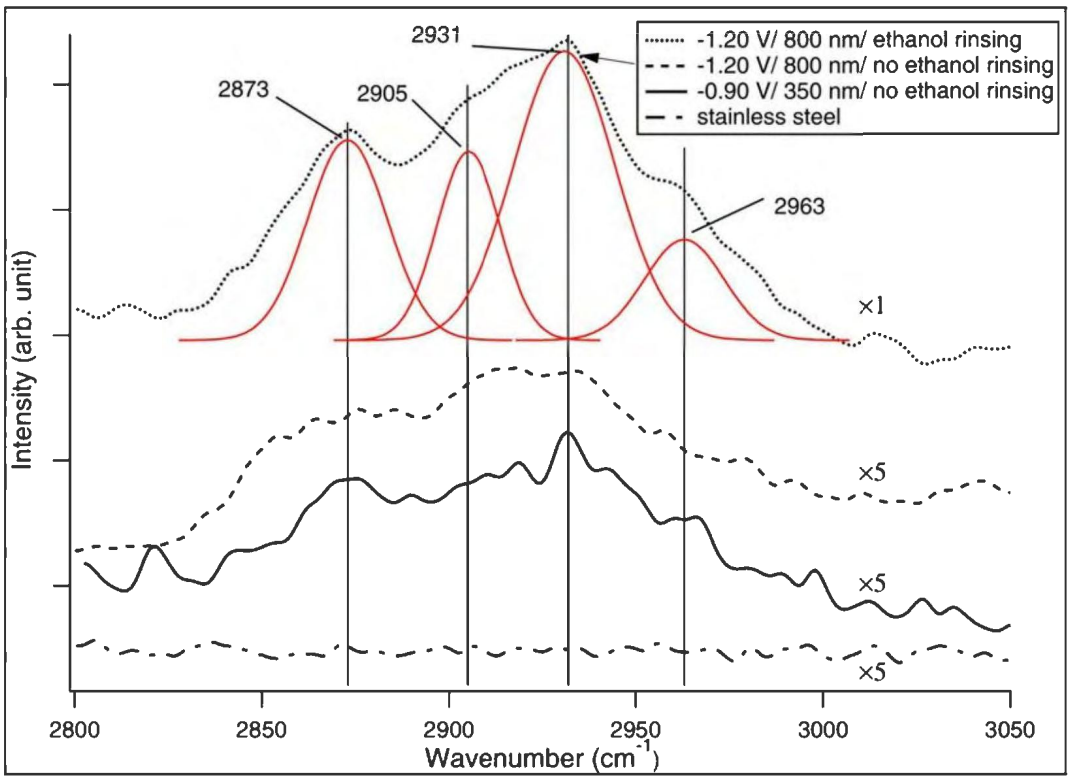

Figure 5.7: Raman spectra for ZnO thin films and the stainless steel substrate in the hydrogen local vibration mode region.

Since Raman data in the 2800 – 3200 cm^{-1} region does not give any conclusive information about hydrogen incorporation, we also investigated in the fingerprint region (300 cm^{-1} – 600 cm^{-1}) for film thickness, applied potential, and sample aging effects. Strong Raman peaks were observed at 436 cm^{-1}, which can be assigned to the E2 (high) ZnO phonon modes [62, 71, 72]. This peak position did not shift with film thickness, deposition potential, or aging time. The A1 (TO) mode was observed at 377 cm^{-1} [63]. There is a broad peak at 331 cm^{-1} attributed to a multi-phonon process [58]. A1 (LO) and E1 (LO) were observed as a broad peak near 580 cm^{-1} which is related to general crystal defect levels (point, line, and plane defects) [58, 59, 57]. Although this peak does not give direct information on hydrogen, it sheds light on the relative defect levels in our ZnO films. For the defect level comparison of ZnO thin films, the intensity of the defect-related phonon mode near 580 cm^{-1} is compared with the E2 (high) mode (related to the deposit (002) crystallinity [57]).

Figure 5.8 shows Raman spectra for a fresh and aged ZnO thin film. The defect level peak did not change substantially after aging. This suggests that the bandgap energy change with aging is not affected by the defect level in ZnO films. A possible explanation for the bandgap energy dependence on aging time is that defects in ZnO deposits are trapping sites for hydrogen. While hydrogen can diffuse out of ZnO [34], the trapping sites would remain. Therefore, the bandgap energy can be reduced by the diffusion of hydrogen, with no change in the overall defect level. Consistent with our bandgap change time scale, Izaki *et al.* [69] reported that ZnO resistivity changes

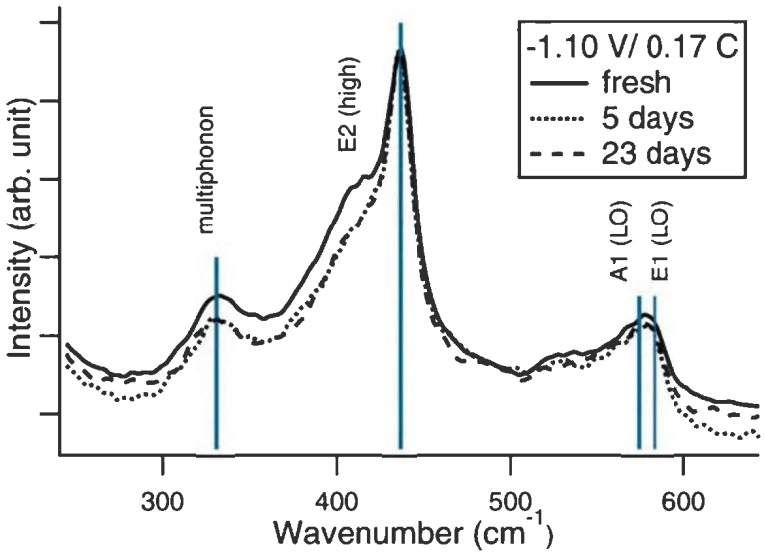

Figure 5.8: Raman spectra for fresh and aged ZnO thin film prepared at –1.10 V.

in the first 200 hours, and by doping ZnO with In, deposits' electronic properties can be stabilized. Jokela *et al.* [68] observed decreased intensity in hydrogen modes from infrared data, associated with a decrease in carrier density after aging several weeks.

Figure 5.9(a) shows representative Raman spectra for electrodeposited ZnO thin films of similar thickness (1 μm $\pm$ 200 nm) with different deposition potentials. This shows that defect levels, inferred from the intensity changes in the defect mode, are higher for deposits prepared at more negative potentials, which also have higher bandgap energies. Figure 5.9(b) shows representative Raman spectra for ZnO thin films electrodeposited at the same potential (–1.00 V) with different thicknesses. Again, the changes in the intensity of the defect mode suggests higher defect levels in thinner films, which also have higher bandgap energies. Thus, optical bandgap

energies of our electrodeposited ZnO are proportional to the defect levels inferred from Raman spectroscopic data.

A possible explanation for this bandgap *vs.* defect level dependence is that there are more hydrogen-trapping sites produced in ZnO films at higher ZnO deposition rates. Figure 5.6 shows there is more charge passed, implying higher ZnO electrodeposition rates, at more negative potentials. Therefore, it is reasonable to propose that there are more trapping sites produced at more negative potentials and in thinner ZnO films. More hydrogen could be incorporated at the trapping sites in ZnO films and increase the bandgap via the Moss-Burstein effect.

Another possible reason for the thickness-induced bandgap change is metal Zn layers at the beginning stage of the ZnO electrodeposition, which are then converted to ZnO. The oxidation of first few metal Zn layers have been reported for ZnO electrodeposition in $Zn(Cl)_2$ electrolytes [73]. It is possible that the first few layers of Zn metal oxidized to ZnO have a higher defect level and cause a bandgap shift. More detailed studies on prelayer influence on ZnO morphology and crystallinity are discussed in Chapter 6.

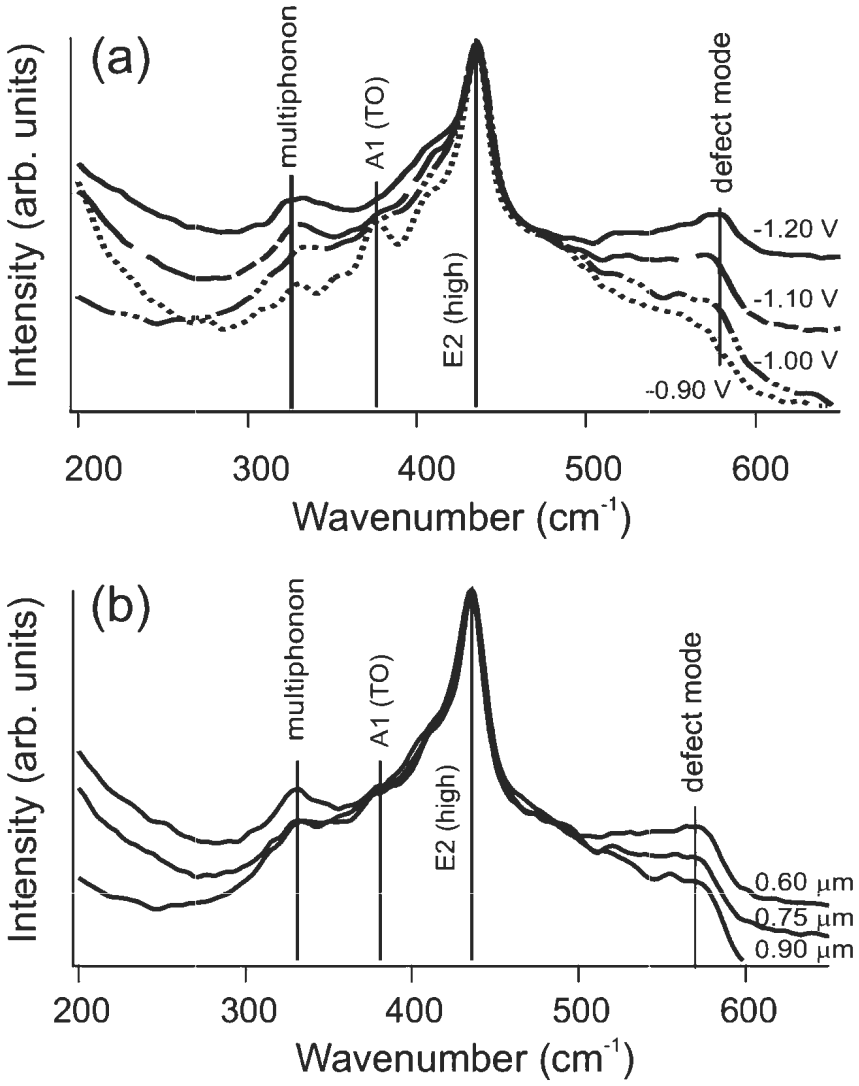

Figure 5.9: Raman spectra of ZnO electrodeposits prepared (a) at different applied potentials with similar thicknesses and (b) at –1.00 V with different thicknesses.

Chapter 6

Monitoring ZnO Crystal Nucleation and Growth

Crystal nucleation and growth are closely related to materials' optical properties. For example, smaller ZnO crystallites ($\leq$ 2 nm) show higher bandgap energies due to quantum confinement effects [48]. This Chapter presents preliminary results when different substrates and different concentrations of additives were used in an attempt to induce different ZnO crystallite growth. *In-situ* AFM was also used to investigate ZnO crystallite formation during electrodeposition.

6.1 Substrate and Prelayer Influence on Electrodeposited ZnO Morphology

Substrates play a large role in electrodeposited ZnO crystal nucleation and growth. Generally speaking, for the substrate influence on ZnO morphology, single crystal substrates can induce better electrodeposited ZnO crystal morphology and size homogeneity than polycrystalline substrates. In the past 10 years, single crystal gold

substrates [51], GaN substrates [74], and silicon substrates [75] were widely used to electrodeposit zinc oxide thin films. However, due to the extreme cost of single crystal substrates, cheap production of zinc oxide, and the benefit of polycrystalline ZnO for solar cell applications [33], most zinc oxide studies in recent years use polycrystalline substrates, such as indium doped SnO_2 (ITO) [38] and gold/glass [36].

6.1.1 Substrate Influence on ZnO Nucleation and Growth

Stainless steel was chosen as the primary substrate for this thesis work, due to the uniform ZnO films which can be electrodeposited on it and its stability in electrolytes of interest. Several other metal polycrystalline substrates were also used to study their effect on electrodeposited ZnO crystallite morphologies.

Figure 6.1(a-c) shows morphologies of ZnO films electrodeposited at –0.90 V for 10 minutes on different substrates. On stainless steel, the ZnO crystallite morphology shows open-structure hexagonal rods with uniform sizes. On regular steel, ZnO crystallites are more closely packed hexagonal rods, but crystallite sizes are not uniform at different spots on the sample. On brass, ZnO deposits do not have a clear and reproducible morphology. Because there is barely any deposit on aluminum substrates at potentials more positive than –1.10 V, an SEM image of ZnO deposits on aluminum substrates prepared at –1.10 V for 10 minutes is shown (Figure 6.1(d)) with large clusters of blade-like crystallites. XRD patterns of ZnO deposits on aluminum show poor preferred crystal orientations.

Some substrates are not stable in the potential region used ZnO electrodeposition. For example, aluminum can be stripped at potentials more negative than –0.50 V in 0.05 M [Cl^-] electrolytes (pH $\sim$ 5). Regular steel substrates form a black coating at potentials more negative than –1.00 V in 0.02 M [NO_3^-] electrolytes (pH $\sim$ 5). Stainless steel is stable in both Cl^- and NO_3^- electrolytes within the potential range we used for ZnO electrodeposition.

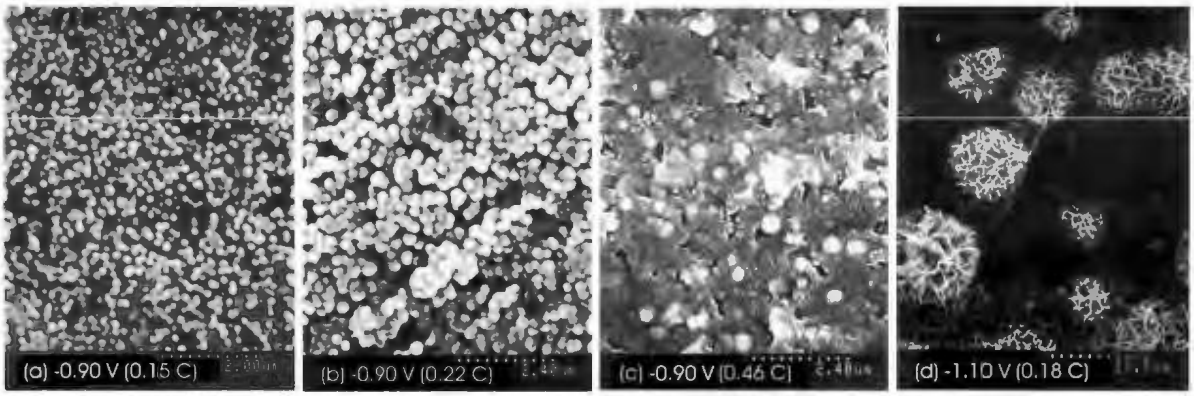

Figure 6.1: ZnO deposition on (a) stainless steel, (b) regular steel, (c) brass, and (d) aluminum substrates. Applied potential and charge passed during electrodeposition are noted on the images.

The charge passed during the 10 minutes of ZnO electrodeposition at –0.90 V (Figure 6.1) on stainless steel is smaller compared to steel and brass. This is probably because the stainless steel formed a thin chromium oxide layer instantly in air, which functions as a potential barrier and slows the ZnO deposition rate. On aluminum, there was no electrodeposit until applied potentials were more negative than –1.10 V, likely due to the aluminum oxide layer formed instantly in air functioning as a potential barrier. However, the fundamental reasons for the ZnO crystallite morphology

variance on different substrates were beyond the scope of this thesis work.

6.1.2 Prelayer Influence on ZnO Nucleation and Growth

In order to further our study of the substrate influence on ZnO morphologies, prelayers were investigated, because topography and composition of a prelayer affect ZnO electrodeposit nucleation. Many literature reports have studied different prelayers, but no conclusive reason for ZnO morphology difference was drawn. Yoshida *et al.* [38] reported hexagonal crystallites for electrodeposited ZnO thin film on an electrodeposited ZnO prelayer. Yamabi *et al.* [21] reported thermally deposited ZnO films on a ZnO amorphous or crystalline undercoat. Canava *et al.* [73] reported that metal Zn layers are deposited in the beginning stages of ZnO electrodeposition in $Zn(Cl)_2$ electrolytes.

Figure 6.2(a) shows an SEM image of ZnO deposits prepared at –0.90 V for 10 minutes on a stainless steel substrate. Figure 6.2(b) shows ZnO deposits prepared at –1.50 V for 30 seconds, which have a plate-like crystallite morphology. Figure 6.2(c) shows a ZnO film prepared by pulsing 10 seconds at –1.50 V, followed by 10 minutes at –0.90 V. The ZnO crystallites in (c) are slightly bigger and have fewer voids.

Figure 6.3 shows XRD data for the three deposits shown in Figure 6.2. The preparation conditions are noted in the figure. Figure 6.3(b) has only one characteristic XRD peak; it could belong to the standard patterns of either ZnO (36.253°/ JCPDS #36-1451) or Zn (36.297°/ JCPDS #04-0831). Therefore, XRD data alone cannot

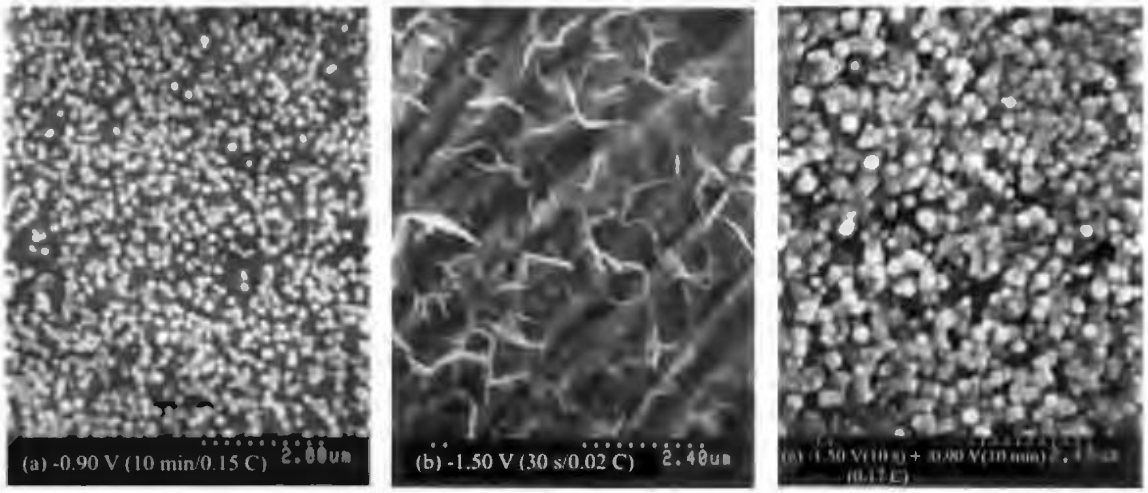

Figure 6.2: ZnO deposits on stainless steel substrates with different applied potentials (deposition time in parentheses) (a) –0.90 V (10 minutes) (b) –1.50 V (30 seconds) (c) –1.50 V (10 seconds) and –0.90 V (10 minutes). The total charge passed through the working electrode during electrodeposition is noted in the images.

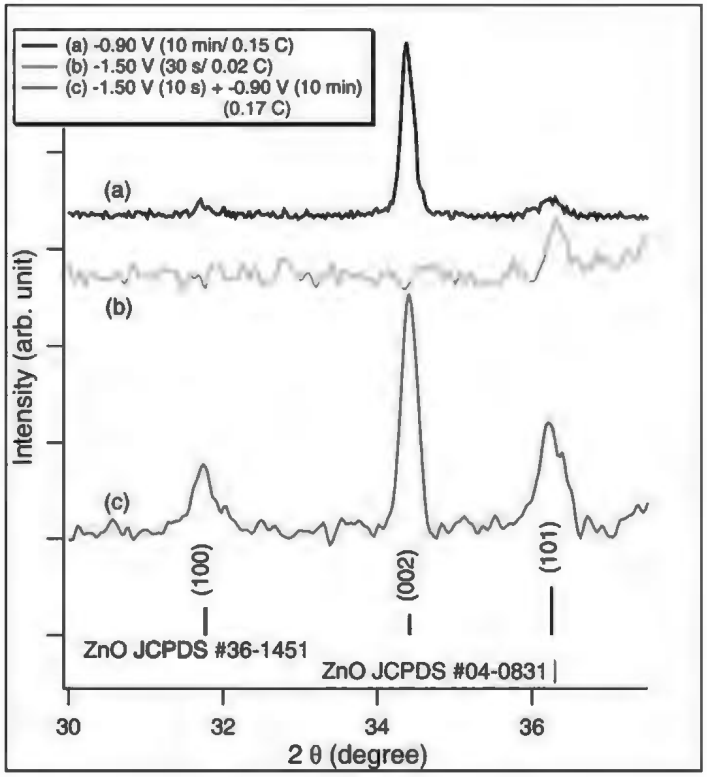

Figure 6.3: XRD data for ZnO electrodeposits with and without a prelayer.

confirm the phase of the deposit. Figure 6.3(a,c) both have characteristic ZnO Bragg peaks. However, Figure 6.3(c) has stronger (100) and (101) orientations than Figure 6.3(a), which indicates less preferred (002) orientation. This suggests that the stainless steel is an excellent substrate for electrodepositing ZnO with preferred (002) orientation without a prelayer.

6.2 Sulfate Additive Influence on ZnO Morphology and Preferred Orientation

Studies by others have demonstrated that additives to an electrolyte can also impact the growth of ZnO thin films. Many additives have been used so far, including trisodium phosphate [76], sodium dodecyl sulfate (SDS) [77] and potassium chloride [25]. Imai *et al.* [76] have reported that 0.001 M phosphate can enlarge the diameter ZnO hexagonal rods and suppress growth along the *c*-axis, while still maintaining a perpendicular orientation of the *c*-axis with respect to the substrate. Li *et al.* [77] reported that 0.01 M SDS can lead to a nut-like twin-structure, which is oriented randomly with respect to the substrate. Xu *et al.* [25] have found that the presence of 0.06 M KCl can change 0.5 μm-diameter hexagonal rods perpendicular to the substrate into 10 μm-diameter ZnO platelets with random orientations.

The most reasonable explanation for the additive's function on the morphology is the adsorption mechanism. Anionic additives tend to absorb on the (0001) ZnO face to retard the growth along *c*-axis, thereby yielding larger-diameter platelets. However,

no answer is available for the additive-induced crystal growing orientation changes so far.

In our experiments, 0.05 M $Zn(NO_3)_2$ served as the source of nitrate and zinc ions. To explore the effect of additives, sodium sulfate decahydrate ($Na_2SO_4 \cdot 10H_2O$) was added to the zinc nitrate electrolyte during some experiments. The molar ratio of SO_4^{2-} to Zn^{2+} in the electrolyte (R) was varied ($0 \leq R \leq 0.02$). The substrate was regular steel. As shown in Figure 6.4, the crystal morphology changes from hexagonal rods (200 nm diameter) to blades (1 μm length) by adding small amounts of sulfate (R=0.02).

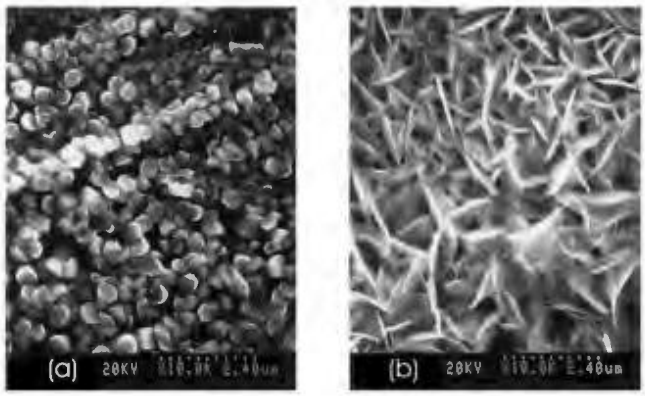

Figure 6.4: SEM images of wurtzite ZnO thin films deposited from 0.05 M zinc nitrate electrolytes at –0.70 V (a) without and (b) with a small concentration of sulfate (R = 0.02). Both depositions were done at 70°C for 10 minutes.

Figure 6.5 shows the XRD patterns for electrodeposits from sulfate-free and sulfate-containing electrolytes. The sulfate-free electrolytes produce phase-pure wurtzite ZnO, but sulfate-containing electrolytes (R=0.02) produce ZnO and a secondary phase marked with asterisk (*).

The morphological change in the presence of sulfate is likely related to the formation of a secondary Zn-containing sulfate phase which affects ZnO nucleation and growth. Characterization methods such as UV-Vis, Raman spectroscopy, IR, Energy dispersive X-ray analysis (EDX) have been used in an attempt to find out what the second phase from the sulfate electrolytes is and how it is incorporated with the ZnO phase. However, our measurements did not give conclusive results. High resolution transmission electron microscopy studies would likely provide more definitive information on the short range crystalline order in this secondary phase.

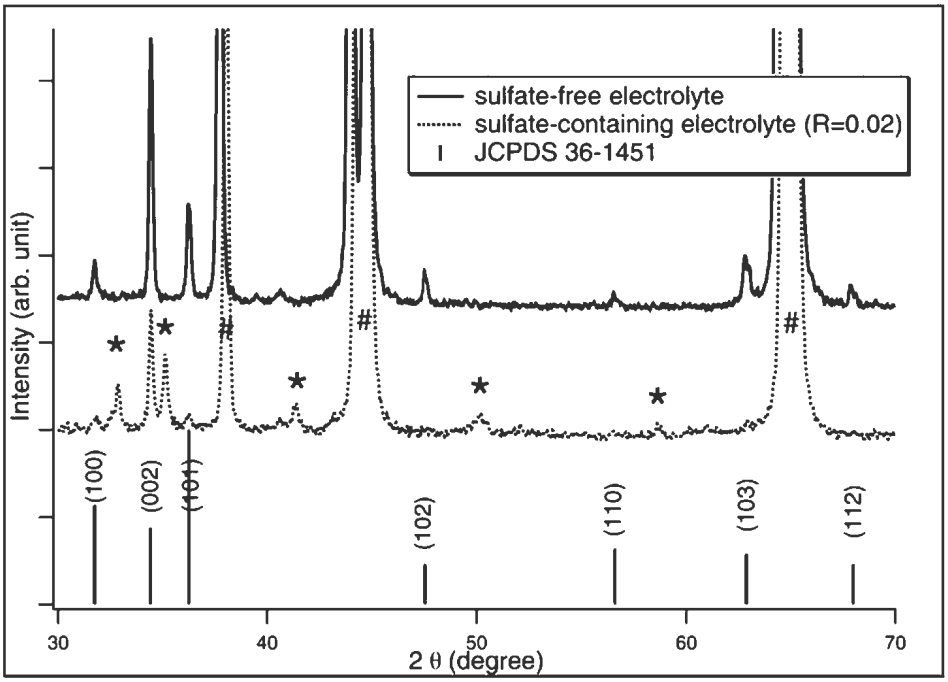

Figure 6.5: XRD data for electrodeposits prepared from electrolytes without (solid) and with (dotted) a small amount of sulfate ions (R= 0.02), at –0.70 V. In the XRD patterns, peaks due to the wurtzite-type ZnO phase are labeled with their *hkl* indices. Peaks from a secondary phase in deposits prepared from the sulfate-containing electrolyte are marked with asterisks (*). Substrate (steel) and sample holder (aluminum) peaks are marked (#).

6.3 AFM Study of *In situ* Crystal Growth

Early stage crystal growth information is important for our prelayer study and for the study of crystal formation. In order to study crystal growth during the electrodeposition, *in situ* AFM was used to monitor room temperature ZnO electrodeposition in a microcell developed in conjunction with Asylum Research (Santa Barbara, California, U.S.A.). As shown in Figure 6.6, the counter electrode is a Pt wire sitting in a groove on a plastic (Kel-F) cell body. The reference electrode (Ag/AgCl) is inserted into a hole on the Kel-F cell mask, and the working electrode is a brass substrate which is electrically connected to the potentiostat via an aluminum bolt. The microcell body holds $\sim$ 2 ml of electrolyte (here, 0.01 M $Zn(NO_3)_2$).

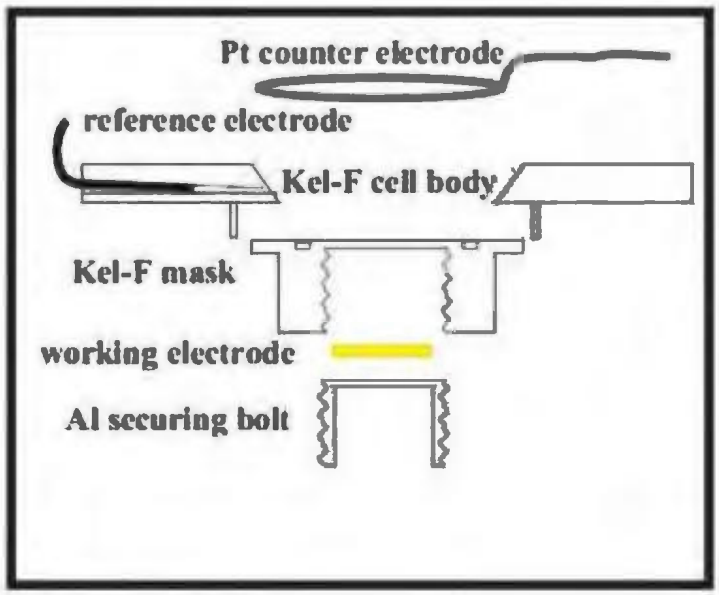

Figure 6.6: Schematic illustration of the *in situ* AFM cell.

Figure 6.7(a) shows an AFM image for the beginning stage of *in situ* electrodeposition at –0.20 V, which shows a clear brass substrate. Figure 6.7(b) represents an AFM image after depositing at –1.00 V for 2 minutes, then at –0.20 V for the image scan. It shows plate-like features which were lost after about 20 minutes at –0.20 V (Figure 6.7(c)), due to the rapid increase in deposit formation. The rapidly formed deposits are flaky and tend to adhere to the AFM tip, so that AFM images become too streaky to interpret. We presume this is due to hydroxide phases that tend to form during room temperature depositions [22].

To solve this problem of hydroxide formation, higher temperature (50°C – 90°C) *in situ* deposition can be used. However, the electrolyte evaporates quickly in our *in situ* microcell. The evaporation problem can be avoided by using a cover for the microcell. It is also hard to purge argon gas into the electrolyte to remove hydrogen, because it will seriously disturb the AFM scan. A solution to degas the oxygen is to use a live electrolyte cell, which input and output electrolytes slowly and continuously during the electrodeposition. These challenges make the microcell design complicated, but would be possible to realize the *in situ* crystal growth monitoring in the future.

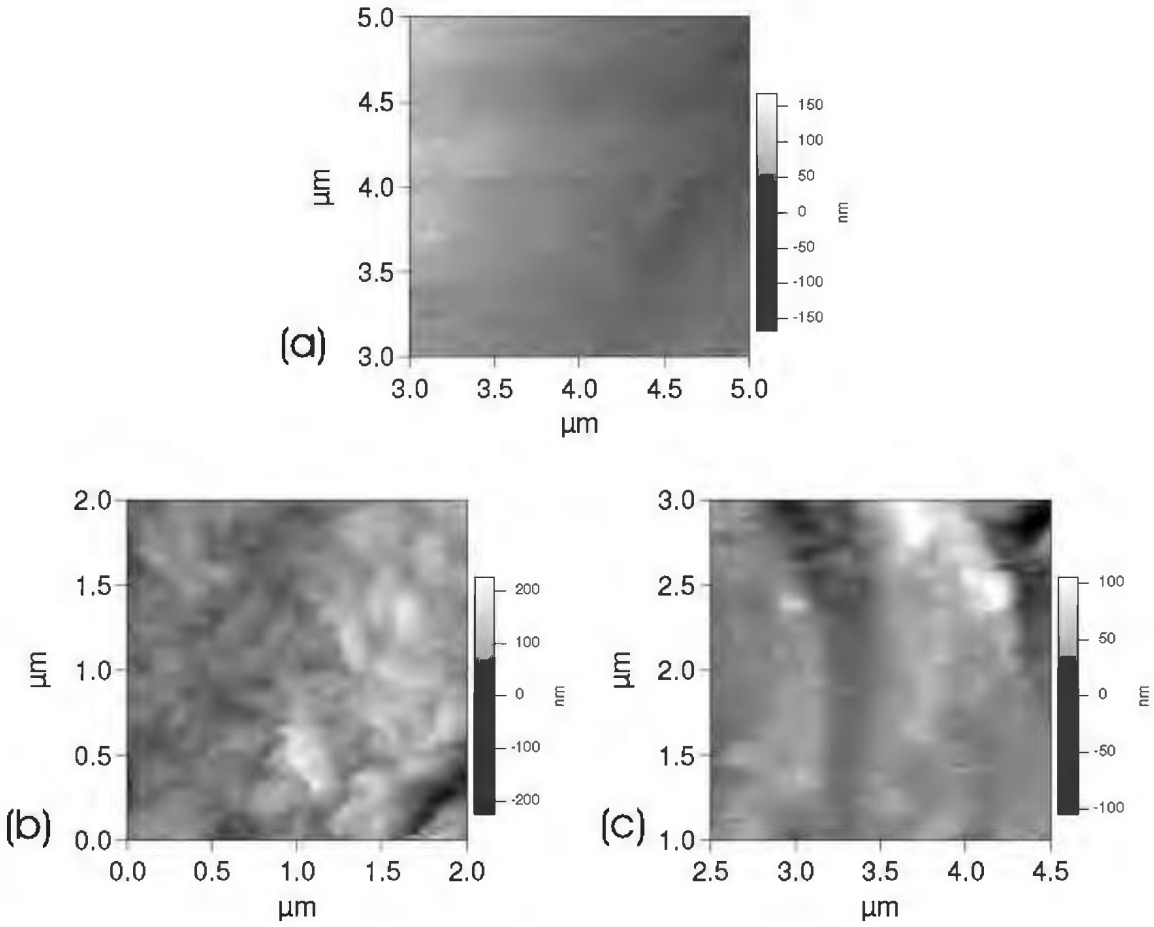

Figure 6.7: *In situ* AFM images of (a) a brass substrate, (b) plate-like electrodeposits, and (c) poorly-imaged electrodeposits (due to deposit pieces sticking to the AFM tip).

Chapter 7

Conclusions

7.1 Conclusions

This thesis work marks the first report of hydrogen studied as a dopant in electrodeposited ZnO. Raman data for sample aging suggest that there are secondary-defects in electrodeposited ZnO which is responsible for hydrogen trapping, consistent with very recent theoretical studies of defect-inhibited hydrogen diffusion in ZnO [34]. This has important implications for long term stability of hydrogen-doped ZnO prepared by any method.

This thesis work also shows that different types of ZnO crystallite morphologies can be achieved by controlling electrodeposition potential. ZnO crystallite size can be increased using longer deposition time. Diffuse reflectance spectroscopic data and Raman spectroscopic data show both potential- and thickness-dependent changes in defect levels and absorption edges, which suggests that H+ can be trapped in secondary defects. Such defects also increase the diffusion time for H+ and lead to

the observed decay in absorption edge energy with aging. Therefore, the most effective way to tune the ZnO bandgap energy is not to change the amount of hydrogen in the electrodeposition environment, but to change the concentration of trapping sites. Trapping site densities can be changed either by altering the electrodeposition kinetics (with applied potential, electrolyte composition, or deposition temperature) or by using thermal post-treatment. Monitoring the ZnO crystallite nucleation and growth provides the possible explanations for the hydrogen-trapping site levels in different thickness films that guides the bandgap energy tuning and electrical conductivity, both of which are important for thin film transistor applications.

7.2 Future studies

Raman data in our film thickness and applied potential study (Chapter 5) suggest different levels of defects in ZnO films. If it is primarily the defects that trap the hydrogen, the different hydrogen amounts in our electrodeposition environment should not have an impact on the bandgap energy. To check this hypothesis one could purge argon through the cell, as usual, and electrodeposit ZnO at a constant potential. In a second experiment, one could change the argon to forming gas ($\leq$ 10% H_2 in N_2), so that there is more hydrogen in the electrodeposition environment. The defect levels in these two samples would be determined by the electrodeposition kinetics, and should be the same. Then one could compare the bandgap of these two ZnO samples to see if more hydrogen is incorporated in electrodeposits with the forming gas purging.

Another interesting issue that arose in this thesis is that SEM images show increase in crystallite sizes with film thickness (Chapter 4). However, the calculated values from XRD peak width and positions have no appreciable change with thickness or applied potential, and are an order of magnitude smaller than the crystallites observed by SEM. This suggest the crystallites shown in SEM images are not single crystals. In order to confirm this, *in-situ* AFM could be used to monitor the ZnO crystallite growth during the electrodeposition process, or and cathodoluminescence could be used to image the crystallite boundaries [78].

In this thesis work, native crystal defects are closely related to ZnO's bandgap energy and other optical properties. Therefore, altering the defect level in ZnO offers another way to tune the bandgap energy. More extensive work can be done to elucidate what the defects are and how the defects trap the hydrogen. This will give more control for using ZnO as an *n*-type thin film transistor material.

Bibliography

[1] G. Moore, Electronics **38**(8) (1965).

[2] D. A. Muller, Nature Materials **4**, 645 (2005).

[3] E. Fortunato, P. Barquinha, A. Pimentel, A. Goncalves, A. Marques, and R. Martins, Advanced Materials **17**(5), 590 (2005).

[4] S. Masuda, K. Kitamura, Y. Okumura, S. Miyatake, H. Tabata, and T. Kawai, Journal of Applied Physics **93**(3), 1624 (2003).

[5] R. L. Hoffman, B. J. Norris, and J. F. Wager, Applied Physics Letters **82**(5), 733 (2003).

[6] B. J. Norris, J. Anderson, J. F. Wager, and D. A. Keszler, Journal of Physics D **36**, L105 (2003).

[7] J. Nishii, F. M. Hossain, S. Takagi, T. Aita, K. Saikusa, Y. Ohmaki, I. Ohkubo, S. Kishimoto, A. Ohtomo, T. Fukumura, *et al.*, Japanese Journal of Applied Physics **42**, L347 (2003).

[8] M. Shur, *Physics of Semiconductor Devices.* (Englewood Cliffs, NJ: Prentice Hall, 1990).

[9] Y. R. Ryu, W. J. Kim, and H. W. White, Journal of Crystal Growth **219**(4), 419 (2000).

[10] D. C. Look, Materials Science and Engineering **B80**, 383 (2001).

[11] M. K. Jayaraj, A. Antony, and M. Ramachandran, Bulletin of Materials Science **25**(3), 227 (2002).

[12] R. Marotti, D. Guerra, C. Bello, G. Machado, and E. Dalchiele, Solar Energy Materials and Solar Cells **82**, 85 (2004).

[13] C. Klingshirn, Physica Status Solidi B **71**(2), 547 (1975).

[14] D. Kan, T. Terashima, R. Kanda, A. Masuno, K. Tanaka, S. Chu, H. Kan, A. Ishizumi, Y. Kanemitsu, Y. Shimakawa, *et al.*, Nature Materials **4**, 816 (11 2005).

[15] M. Kumar, R. M. Mehra, A. Wakahara, M. Ishida, and A. Yoshida, Journal of Applied Physics **93**(7), 3837 (2003).

[16] D. M. Bagnall, Y. F. Chen, Z. Zhu, T. Yao, S. Koyama, M. Y. Shen, and T. Goto, Applied Physics Letters **70**, 2230 (1997).

[17] P. Li, Y. Wei, H. Liu, and X. Wang, Journal of Solid State Chemistry **178**, 855 (2005).

[18] Y. G. Wang, S. P. Lau, H. W. Lee, S. F. Yu, B. K. Tay, X. H. Zhang, and H. H. Hng, Journal of Applied Physics **94**(1), 354 (2003).

[19] M. Izaki and T. Omi, Applied Physics Letters **68**(17), 2439 (1996).

[20] I. M. Dharmadasa and J. Haigh, Journal of The Electrochemical Society **153**(1), G47 (2006).

[21] S. Yamabi and H. Imai, Journal of Materials Chemistry **12**, 3773 (2002).

[22] A. Goux, T. Pauportè, J. Chivot, and D. Lincot, Electrochimica Acta **50**, 2239 (2005).

[23] M. Izaki and T. Omi, Journal of the Electrochemical Society **143**(3), L53 (1996).

[24] T. Mahalingam, V. John, M. Raja, Y. Su, and P. Sebastian, Solar Energy Materials and Solar Cells **88**, 227 (2005).

[25] L. Xu, Y. Guo, Q. Liao, J. Zhang, and D. Xu, Journal of Physical Chemistry B **109**, 13519 (2005).

[26] N. R. Aghamalyan, I. A. Gambaryan, E. K. Goulanian, R. K. Hovsepyan, R. B. Kostanyan, S. I. Petrosyan, E. S. Vardanyan, and A. F. Zerrouk, Semiconductor Science and Technology **18**(6), 525 (2003).

[27] A. Ohtomo, M. Kawasaki, T. Koida, H. Koinuma, Y. Sakurai, Y. Yoshida, M. Sumiya, S. Fuke, T. Yasuda, and Y. Segawa, Materials Science Forum **264-268**, 1463 (1998).

[28] L. M. Kukreja, S. Barik, and P. Misra, Journal of Crystal Growth **268**, 531 (2004).

[29] T. Pauportè and D. Lincot, Electrochimica Acta **45**, 3345 (2000).

[30] V. Srikant and D. R. Clarke, Journal of Applied Physics **81**(9), 6357 (1997).

[31] D. Gal, Y. Mastai, G. Hodes, and L. Kronik, Journal of Applied Physics **86**(10), 5573 (1999).

[32] R. E. Marotti, P. Giorgi, G. Machado, and E. A. Dalchiele, Solar Energy Materials and Solar Cells **90**, 2356 (2006).

[33] B. Oh, M. Jeong, D. Kim, W. Lee, and J. Myoung, Journal of Crystal Growth **281**, 475 (2005).

[34] M. G. Wardle, J. P. Goss, and P. R. Briddon, Physical Review Letters **96**, 205504 (2006).

[35] J. A. Switzer, American Ceramic Society Bulletin **66**(10), 1521 (1987).

[36] S. Peulon and D. Lincot, Journal of the Electrochemical Society **145**(3), 864 (1998).

[37] M. Pourbaix, *Atlas of electrochemical equilibria in aqueous solutions.* (Pergamon Press, New York, 1996).

[38] T. Yoshida, D. Komatsu, N. Shimokawa, and H. Minoura, Thin Solid Films **451-452**, 166 (2004).

[39] J. A. Dean, *Lange's Handbook of Chemistry.* (McGraw-Hill, New York, 1992), 14th ed.

[40] J. Lee and Y. Tak, Electrochemical and Solid-State Letters **4**(9), 63 (2001).

[41] E. Burstein, Physical Review **93**(3), 632 (1954).

[42] K. S. A. Butcher, H. Hirshy, R. M. Perks, M. Wintrebert-Fouquet, and P. P-T Chen, Physica Status Solidi A **203**(1), 66 (2006).

[43] B. E. Sernelius and K. F. Berggren, Physical Review B **37**(17), 10244 (1988).

[44] D. Song, P. Widenborg, W. Chin, and A. G. Aberle, Solar Energy Materials and Solar Cells **73**, 1 (2002).

[45] S. J. Baik, J. H. Jang, C. H. Lee, W. Y. Cho, and K. S. Lim, Applied Physics Letters **70**(26), 3516 (1997).

[46] J. Hu and R. G. Gordon, Journal of Applied Physics **72**(11), 5381 (1992).

[47] Y. Cao, L. Miao, S. T. Y. Hayashi, and M. Tanemura, Advanced Materials Research **11-12**, 159 (2006).

[48] Y. Gu, I. Kuskovsky, M. Yin, S. O'Brien, and G. Neumark, Applied Physics Letters **85**(17), 3833 (2004).

[49] A. J. Bard and L. R. Faulkner, *Electrochemical Methods: Fundamentals and Applications* (John Wiley and Sons Inc., New York, 2001), 2nd ed.

[50] D. Bizzotto, *World Wide Web: www.chem.ubc.ca/personnel/faculty/bizzotto.* (Last accessed July 2006).

[51] R. Liu, A. Vertegel, E. Bohannan, T. Sorenson, and J. Switzer, Chemistry of Materials **13**, 508 (2001).

[52] Joint Commission on Powder Diffraction Standards – International Centre for Diffraction Data, *Powder Diffraction File* (2003), www.icdd.com.

[53] D. Schwarzenbach, *LATCON: Program for the LS-refinement of Lattice Constants* (Uni Lausanne, Switzerland, 1975).

[54] W. Lasocha and K. Lewinski, *Prozski* (World Wide Web, Last accessed July 2006).

[55] L. V. Azaroff and M. J. Buerger, *The Powder Method in X-ray Crystallography.* (McGraw-Hill, New York, 1958).

[56] J. I. Goldstein, D. E. Newbury, P. Echlin, D. C. Joy, C. Fiori, and E. Lifshin, *Scanning Electron Microscopy and X-Ray Microanalysis: A Text for Biologists, Materials Scientists, and Geologists.* (Plenum Press, New York, 1981).

[57] G. W. Cong, H. Y. Wei, P. F. Zhang, W. Q. Peng, J. J. Wu, X. L. Liu, C. M.

Jiao, W. G. Hu, Q. S. Zhu, and Z. G. Wang, Applied Physics Letters **87**, 231903 (2005).

[58] Z. Q. Chen, A. Kawasuso, Y. Xu, and H. Naramoto, Physical Review B **71**, 115213 (2005).

[59] F. Reuss, C. Kirchner, T. Gruber, R. Kling, S. Maschek, W. Limmer, A. Waag, and P. Ziemann, Journal of Applied Physics **95**(7), 3385 (2004).

[60] S. Tripathy, S. J. Chua, P. Chen, and Z. L. Miao, Journal of Applied Physics **92**(7), 3503 (2002).

[61] C. V. Raman and K. S. Krishnan, Nature **121**(501), 3048 (3 1928).

[62] K. A. Alim, V. A. Fonoberov, and A. A. Balandin, Applied Physics Letters **86**, 053107 (2005).

[63] T. C. Damen, S. P. S. Porto, and B. Tell, Physical Review **142**(2), 570 (1966).

[64] G. Riveros, H. Gomez, R. Henriquez, R. Schrebler, R. Cordova, R. E. Marotti, and E. A. Dalchiele, Boletin de la Sociedad Chilena de Quimica **47**, 411 (2002).

[65] J. Lee and J. Maier, Journal of Material Research **20**(8), 2101 (2005).

[66] K. Ip, M. E. Overberg, Y. W. Heo, D. P. Norton, S. J. Pearton, C. E. Stutz, S. O. Kucheyev, C. Jagadish, J. S. Williams, B. Luo, *et al.*, Solid-State Electronics **47**, 2255 (2003).

[67] E. M. Wong and P. C. Searson, Applied Physics Letters **47**(20), 2939 (1999).

[68] S. J. Jokela and M. D. McCluskey, Physical Review B **72**, 113201 (2005).

[69] M. Izaki and Y. Saijo, Journal of The Electrochemical Society **150**(2), C73 (2003).

[70] N. H. Nickel and K. Fleischer, Physical Review Letters **90**(19), 197402 (2003).

[71] F. Decremps, J. Pellicer-Porres, A. M. Saitta, J. Chervin, and A. Polian, Physical Review B **65**, 092101 (2002).

[72] T. Gruber, G. M. Prinz, C. Kirchner, R. Kling, F. Reuss, W. Limmer, and A. Waag, Journal of Applied Physics **96**(1), 289 (2004).

[73] B. Canava and D. Lincot, Journal of Applied Electrochemistry **30**, 711 (2000).

[74] T. Pauportè, R. Cortes, M. Froment, B. Beaumont, and D. Lincot, Chemistry of Materials **14**, 4702 (2002).

[75] E. A. Dalchiele, P. Giorgi, R. E. Marotti, F. Martin, J. R. Ramos-Barrado, R. Ayouci, and D. Leinen, Solar Energy Materials and Solar Cells **70**, 245 (2001).

[76] H. Imai, S. Iwai, and S. Yamabi, Chemistry Letters **33**(6), 768 (2004).

[77] P. Li, Y. Wei, H. Liu, and X. Wang, Journal of Solid State Chemistry **178**, 855 (2005).

[78] T. Nobis, E. M. Kaidashev, A. Rahm, M. Lorenz, J. Lenzner, and M. Grundmann, Nano Letters **4**(5), 797 (2004).

[79] D. Schwarzenbach, S. C. Abrahams, H. D. Flack, W. Gonschorek, T. Hahn, K. Huml, R. E. Marsh, E. Prince, B. E. Robertson, and J. Wilson, Acta Cryrstallographica **A45**, 63 (1989).

Appendix A

Procedure for Using LATCON to Refine Lattice Constants

The process of obtaining lattice constants from XRD data is done through peak position fitting and lattice constant refinements. A peak fitting macro fits each XRD peak with a Gaussian function to give the position of the peak maxima. The procedure for obtaining the peak positions with the assistance of Igor Pro (Wavemetrics, Inc.) is listed below.

- In Igor Pro, load the XRD pattern using the procedure mdiloader.ipf designed by Bryan Jerrett, a former group member.

- In the Analysis tab⇒package⇒multipeak fitting, a panel called FitSetupPanel appears.

- In the FitSetupPanel, choose Y as the XRD pattern wave and X as calculated. Use the **set** option to give the XRD pattern a group of automatically fitted

peaks. Use the **Graph** option to see the fitting residue. The goal of fitting the peaks is to reduce the residue to the minimum. If the **Set** option does not give all the peaks needed, peaks can be added menually using the **Man** option.

- Choose the fitting fuction as Gaussian. Do Fit. Run Do Fit several times to get a good fit.

- The peak position value can be obtained from the **position** option in this FitSetupPanel.

LATCON refines the best value for lattice constants using least-squares method [53, 79]. LATCON input files require the following parameters: the XRD peak positions, their *hkl* indexes, X-ray source wavelength (1.54056 Å), and crystal class (hexagonal for ZnO).

- Choose "new active file", and give the name of the XRD pattern. If the file name is not found, you will be asked if you want to create this file. (choose Y)

- Choose "update parameters". Put in the title, radiation source wavelength (1.54056 Å), symmetry (hexagonal), and the Bragg peak positions (2θ to 4 significant figures) [space group and space group number are optional].

- Back to the main menu⇒Lattice constant refinement⇒Refinement by the program LATCON⇒Prepare input file⇒Y⇒Refinement of correction (choose one of three options: No refinement of the 2θ zero shift correction, Refinement of

correction proportional to $\sin(2\theta)$, and Refinement of correction proportional to $\mathrm{ctg}(\theta)$)

- Run Program⇒Browse through results. Lattice constant refinement results show the observed 2θ values, calculated 2θ values, and $\delta(2\theta)$ values. The $\delta(2\theta)$ is the difference between the zero shift modified observed 2θ and calculated 2θ. The choice of refinement of correction can be made to the method which gives the smallest $\delta(2\theta)$ values. A pure-phase substance will have very similar $\delta(2\theta)$ values ($\sim 0.010°$ in our thesis work). However, multiphase substances have Bragg peaks from multiple unit cells, so some peaks will not match with the desired phase's XRD pattern and will have $\delta(2\theta)$ values much bigger than the other peaks. The result file also gives the refined lattice constants with their estimated standard deviations.

Appendix B

Abbreviations and Symbols

Listed in order of first appearance in the thesis.

LCD	liquid crystal display
TFT	thin film transistor
LED	light emitting diode
MBE	molecular beam epitaxy
SCE	saturated calomel electrode
XRD	x-ray diffraction
AFM	atomic force microscopy
SEM	scanning electron microscopy
IR	infrared spectroscopy
UV-Vis	ultraviolet-visible spectroscopy
DRS	diffuse reflectance spectroscopy
WE	working electrode

RE	reference electrode
CE	counter electrode
E *vs.* Ag/AgCl	potential with respect to the Ag/AgCl reference electrode
JCPDS	joint committee for powder diffraction studies
E_g	bandgap energy
λ	wavelength
d	d-spacing between the crystal planes
t	average crystallite size
B	peak width (2θ in rad) at half peak intensity
B_m	measured peak widths at half maxima
B_s	instrumental broadening
θ_B	peak position
$\mathbf{E}$	incident light electric field
$\mathbf{P}$	electric dipole moment
h	Planck's constant
c	speed of light
T	transmittance
α	absorption coefficient